Award Number: W81XWH-10-1-0843

TITLE: In Vivo PET Imaging of Myelin Damage and Repair in the Spinal Cord

PRINCIPAL INVESTIGATOR: Robert H. Miller, Ph.D.

CONTRACTING ORGANIZATION: Case Western Reserve University
Cleveland, OH 44106-7026

REPORT DATE: December 2013

TYPE OF REPORT: Final

PREPARED FOR: U.S. Army Medical Research and Materiel Command
Fort Detrick, Maryland 21702-5012

REPORT DOCUMENTATION PAGE

Form Approved
OMB No. 0704-0188

1. REPORT DATE 1 Dec 2013	**2. REPORT TYPE** Final	**3. DATES COVERED** 30 Sept. 2010–29 Sept.2013

4. TITLE AND SUBTITLE

In Vivo PET Imaging of Myelin Damage and Repair in the Spinal Cord

5a. CONTRACT NUMBER

5b. GRANT NUMBER

W81XWH-10-1-0843

5c. PROGRAM ELEMENT NUMBER

6. AUTHOR(S)
Dr. Robert H. Miller

rhm3@gwu.edu

5d. PROJECT NUMBER

5e. TASK NUMBER

5f. WORK UNIT NUMBER

7. PERFORMING ORGANIZATION NAME(S) AND ADDRESS(ES)

AND ADDRESS(ES)
Case Western Reserve
University
10900 Euclid Ave.
Cleveland Ohio 44106-7026

8. PERFORMING ORGANIZATION REPORT NUMBER

9. SPONSORING / MONITORING AGENCY NAME(S) AND ADDRESS(ES)
U.S. Army Medical Research
And Materiel Command
Fort Detrick, Maryland
21702-5012

10. SPONSOR/MONITOR'S ACRONYM(S)

11. SPONSOR/MONITOR'S REPORT NUMBER(S)

12. DISTRIBUTION / AVAILABILITY STATEMENT

Approved for public release; distribution unlimited

13. SUPPLEMENTARY NOTES

14. ABSTRACT

During the first funding cycle, we have worked closely with Dr Wang to develop a series of animal models to assess the efficacy of the imaging compounds that he has developed to detect demyelination and remyelination in the intact brain and spinal cord. We have also begun to test the ability of the imaging probes to assay remyelination in response to potential therapeutic treatments. The key research accomplishments are highlighted below:

1. Design, synthesis and evaluation of coumarin-based molecular probes for imaging of myelination. (Wang et al, J. Med. Chem. 2011)
2. Longitudinal imaging of myelination using a near infra-red probe. (Wang et al, J. Neuroscience 2011)
3. Longitudinal [^{11}C]CIC-PET Imaging in the spinal cord of a rat model of focal demyelination.

15. SUBJECT TERMS
Positron emission tomography, imaging, myelination, molecular probes, multiple sclerosis.

16. SECURITY CLASSIFICATION OF:			**17. LIMITATION OF ABSTRACT**	**18. NUMBER OF PAGES**	**19a. NAME OF RESPONSIBLE PERSON** USAMRMC
a. REPORT U	**b. ABSTRACT** U	**c. THIS PAGE** U	UU	32	**19b. TELEPHONE NUMBER** *(include area code)*

Standard Form 298 (Rev. 8-98)
Prescribed by ANSI Std. Z39.18

Table of Contents

Page

INTRODUCTION

The project covered by this report reflects a long staining collaboration between Dr. Yanming Wang and Dr. Robert Miller. Dr. Wang is the overall director of the program that has focused on the development of new modalities for longitudinal imaging of white matter in normal and pathological conditions. Dr. Wang is a radiochemist and throughout the course of this work has been responsible for the generation of new compounds that selectively bind to components of the myelin sheath. Dr. Miller is a neuroscientist with extensive experience in glial development, myelin biology and demyelinating diseases. This report is the companion to that of Dr. Wang who describes in detail the generation of the probes and the chemistry related to their binding properties. In this report we have not duplicated this information, but rather focused the report on new information regarding characterization of the novel probes in the setting of the normal CNS and in number of pathological conditions. Our overall progress on this project is reflected in the combination of both reports.

Multiple sclerosis is the most common adult CNS demyelinating disease. It frequently affects young adults and severely compromises the quality of life for affected individual. Recently an increase in the incidence of MS has been reported among US veterans further adding to the burden on society from this disease. Classically the disease is considered to be an autoimmune disease in which cells of the immune system become reactive to white matter components and result in tissue destruction and functional impairment. Specifically, T cells attack myelin sheaths resulting in a loss of axonal conduction. Myelin is the fatty insulation that surrounds axons and protects them from damage. Myelin also enhances the rate of axonal conduction by facilitating saltatory conduction and lowering the threshold for continued axonal conduction. In the brain and spinal cord myelin is generated by cell called oligodendrocytes. These cells develop from defined precursor cells (oligodendrocyte precursor cells (OPCs)) that arise in distinct region of the CNS in response to local signals (Miller 2002). While much has been learned about the biology of the oligodendrocyte lineage during development, our understanding of these cells in the adult CNS is less well understood. One of the most interesting aspects of this lineage is that a large number of OPCs persist in the adult CNS. If these cells retain the potential to differentiate into mature oligodendrocytes and generate new myelin they represent a unique source for myelin repair in disease such as MS.

Current therapies are not however targeted towards stimulating myelin repair in MS but rather directed toward controlling the pathological insults from the systemic immune system. The reason for the immunological focus of therapies is that clear metrics of effectiveness exist for monitoring the efficacy of immune suppressive drugs while no such metrics exist for drugs targeted at myelin repair. Over the last few years it has become clear that suppressing the immune system while necessary, is not sufficient to promote functional recovery in MS and this has driven the field to consider new approaches to stimulate adult OPCs and promote myelin repair. In turn the increasing emphasis on myelin repair has fueled a demand for accurate ways to assess the levels of myelination in non-invasive ways. Myelin is easily assayed in pathological specimens using classical histological approaches, however the ability to image myelin in the intact, living CNS in a longitudinal manner is still significantly underdeveloped. Developing and validating new myelin specific probes has been primary goal of this project and we have made major advances in several areas that are described in these reports. For example, we have generated a range of new molecular myelin imaging probes. We have validated these probes in a number of models and shown we can generate quantitative data on the myelin content of specific CNS regions. We have used both genetic and molecular models to characterize the binding properties of the different probes and perhaps most importantly we

have shown that we can demonstrate the efficacy of therapeutic reagents to promote myelin repair in the intact longitudinal CNS.

BODY

This project was supported through a Synergistic Idea Award from the Department of Defense that brought together leaders in radiochemistry and myelin biology to develop and refine new imaging modalities for CNS myelin and to determine whether such imaging approaches could be used to define the efficacy of novel therapeutic approaches to myelin repair using a range of different animal models. Ultimately, the overall goal of this award is to develop new imaging probes that can be used to monitor the levels of myelination and remyelination in the adult human CNS. These studies begin to allow us to identify the best candidate(s) that are uniquely suited for future clinical trials. We hypothesize that myelin repair can be achieved by therapeutic agents that stimulate the endogenous promotion of remyelination by adult OPCs. Further, we specifically hypothesize that the efficacy of remyelinating agents can be quantified in vivo through direct correlation of the levels of binding of myelin specific probes detected in longitudinal studies with changes in the level of myelination as a result of therapeutic treatment. Our approach has been to initially develop myelin-imaging agents that can monitor longitudinal myelin changes in different animal models of demyelination. This has involved refining the chemistry of the original probes to enhance blood-brain permeability, specificity of the probes for myelin components, enhancing signal to noise ratios and identifying the best reporter systems. In subsequent studies we have used PET imaging to evaluate the in vivo myelin repair properties of recently identified therapeutic agents. We then validate the in vivo studies by correlation with postmortem histology studies. Completion of this project has allowed us to identify the lead candidate for Phase I clinical trials and we are in the process of identifying partners and funding support to undertake this next stage of the program.

Key Research accomplishments

Design, Synthesis and Evaluation of Coumarin-based Molecular Probes for Imaging of Myelination. Wang et al., J Med Chem 2011.

Longitudinal Imaging of Myelination using a near infrared probe. Wang et al J. Neuroscience 2011.

Longitudinal [11C]MeDAS-PET imaging in spinal cord. Wu et al. Annals of Neurology 2013

REPORTABLE OUTCOMES

1. Design, Synthesis and Evaluation of Coumarin-based Molecular Probes for Imaging of Myelination

During the period of support for this program we developed a series of small molecular probes that readily penetrate the blood-brain barrier and selectively bind to myelin with high affinity and specificity. Compared to conventional myelin stains such as Luxol fast blue and fluoromyelin, these molecular probes are capable of direct imaging of myelination *in vivo*. For example, some of these SMPs have been used for positron emission tomography (PET), which is widely used to study biochemical and metabolic changes at molecular level. One of the lead myelin-imaging agents has also been used for myelin imaging in non-human primates. The approach undertaken by Dr. Wang was to design a series of coumarin derivatives as myelin-imaging agents. Coumarin is a natural product occurring in plants and has many important biological activities and we had previously reported a coumarin derivative, 3-(4-aminophenyl)-2H-chromen-2-one, termed CMC, which exhibits promising myelin-binding properties. To fully

examine the potential of this class of compounds as myelin-imaging agents, we evaluated 36 coumarin derivatives through *in vitro* fluorescent tissue staining and *in vivo* fluorescent imaging. To accomplish this analysis we screened these compounds on frozen sections of rat brain and correlated the levels and pattern of binding with the known histology and localization of white matter. Using these approaches Dr. Wang identified some molecular generalities that modulated myelin-binding properties. The detailed structure and synthesis are discussed in detail in his accompanying report. An example of one of these compounds is shown in Figure 1 where selective binding to white matter regions in the forebrain, cerebellum and sciatic nerve are clearly demonstrated.

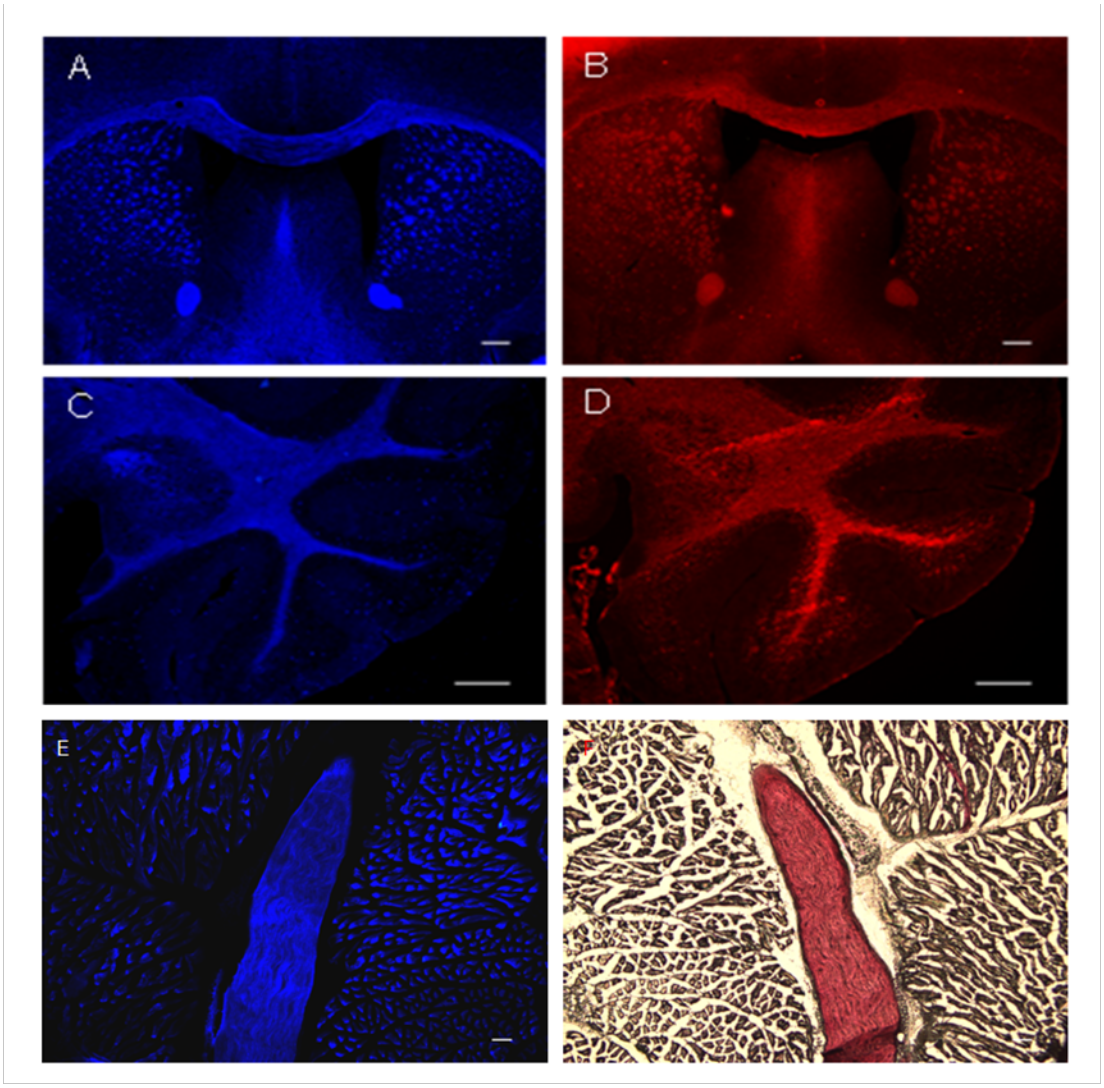

Figure 1. *In vitro* labeling of section of mouse forebrain with compound 32. (A), cerebellum (C), and sciatic nerve (E). For comparison, the same sections were used for MBP staining of the whole mouse brain (B), cerebellum (D) and for Black-gold II staining of sciatic nerves (F). Scale bar: A, B=500 μm, C, D=300 μm, E, F=100 μm

These studies provided confidence that the probes were binding to structures that were highly expressed in white matter; they do not however demonstrate these probes specifically identify myelin components as the targets. To address this issue we utilized a genetic approach in which we assayed the binding of the probes to sections of brain and spinal cord prepared from animals that have a deletion in the Myelin Basic Protein (MBP) gene. These animals are termed *shiverer* as a result of their behavioral phenotype. The central nervous system of *shiverer* animals contains all the elements of the CNS except compact myelin sheaths, because myelin sheath formation depends critically on the presence of MBP. Comparison of probe binding to wild type and *shiverer* sections revealed a profound reduction in the intensity of the probes binding to *shiverer* CNS (Figure 2) demonstrating that the binding target of the probe is specifically associated with compact myelin. Preliminary competitive binding studies suggest that the probe 32 recognizes MBP or some component very closely associated with MBP.

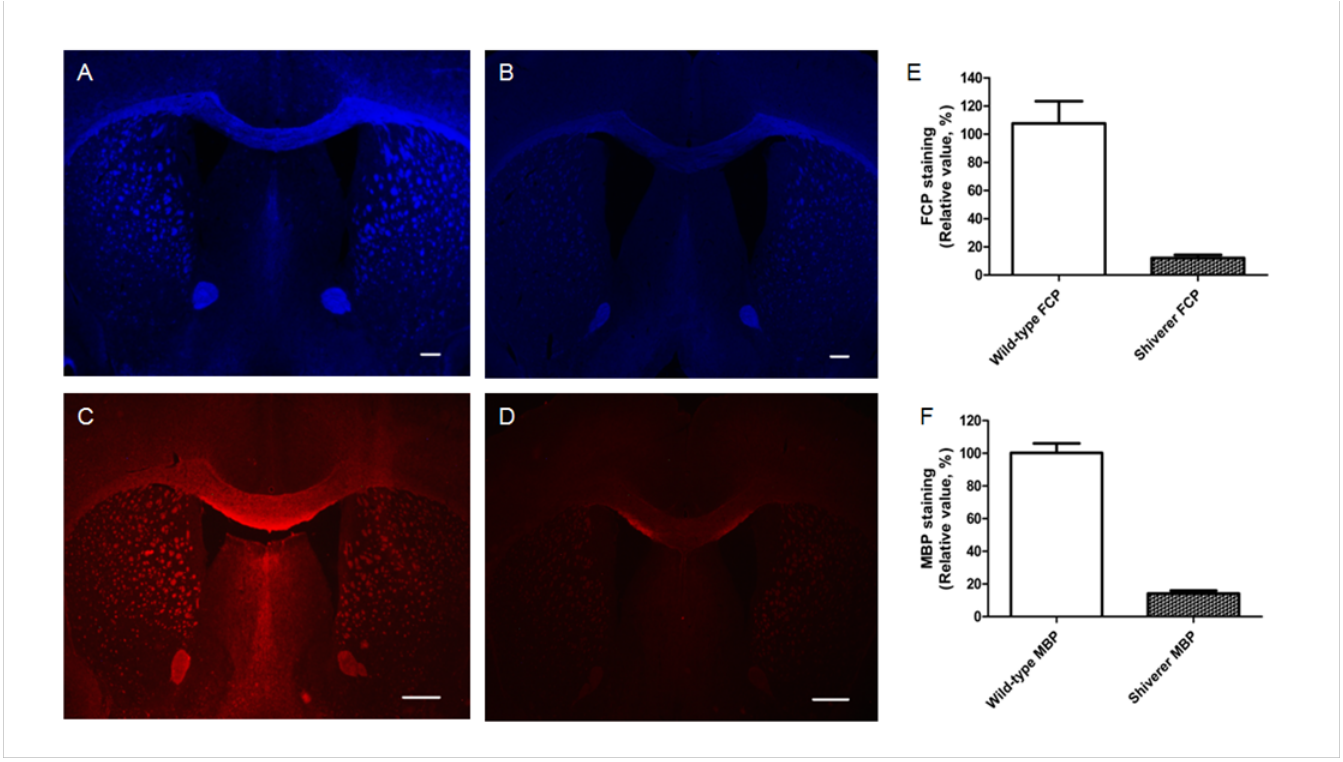

Figure 2. Comparison of 32 staining of the wild-type mouse brain (A) and myelin-deficient *shiverer* mouse brain (B). Staining with anti-MBP of the same brain sections (C, wild-type; D, *shiverer*) was also conducted for comparison. Fluorescent intensities in the same corpus callosum region following MBP staining and 32 staining were quantified. The data were analyzed using a GraphPad Prism. (E) P=0.0005, n=3, Unpaired t-test; (F) P<0.0001, n=3, Unpaired t-test. Scale bar: A, B=300 μm, C, D=500 μm

Regardless of the precise nature of the moiety recognized by probe 32 these studies indicate that this approaches provides for the development of compact myelin specific probes. Such specificity is critical for in vivo studies where the goal is to identify changes in the levels of compact myelin in the intact CNS. One unexpected finding was that the probe 32 not only recognized compact CNS myelin but also selectively labeled compact myelin in the peripheral nervous system (PNS). Myelin in the PNS is generated not by oligodendrocytes but by Schwann cells that have a different ancestral history and use a different combination of

proteins and lipids to generate myelin sheaths. It is known that some isoforms of MBP are shared between the CNS and PNS, but these data may indicate that rather than the specificity of the probe being linked to a single molecular entity, rather it is a reflection of unique structural organization of myelin sheaths whether they are derived from oligodendrocytes or Schwann cells.

One potential use of 32 may be in PET imaging of demyelination. In our previous studies, we identified some lead compounds that readily entered the brain and selectively localized in the myelinated regions. These findings provide proof-of-the-concept that small-molecule myelin-imaging probes can be developed via direct binding to myelin membranes. However, all of these imaging probes are radiolabelled with C-11. Due to short half-life (20 min), C-11-labelled probes can only be synthesized on site using a dedicated cyclotron and are not suitable for remote distribution. Since most of clinical facilities do not have a cyclotron, use of C-11-labelled imaging agents is limited. In order to enhance the potential of their clinical applications, myelin-imaging agents have to be radiolabelled with fluorine-18, a positron-emitting radionuclide with a half-life of 110 min. F-18-Labelled agents are suitable for regional distribution and can be used by PET facilities without an on-site cyclotron. Thus, in future studies, Dr. Wang and Dr. Miller plan to evaluate F-18-labelled 32 for PET studies in a way similar to widely used 2-fluorodeoxyglucose (FDG).

2. Analysis of the binding properties of near infrared myelin binding probes

In addition to probes such as 32, during the course of this program Dr. Wang generated a number of additional probes with different imaging capabilities. One of these is termed DBT. The synthesis and structure of DBT is described in more detail in Dr. Wang's report. To assess the binding properties of DBT in CNS tissues we used a similar strategy to that described for 32 above. Labeling of wild type mouse brain sections revealed that at 1 μM concentration, DBT selectively labeled intact myelin sheaths present in the whole mouse brain, particularly in the corpus callosum and the caudate putman (Figure 3C). The pattern of myelin sheaths stained by DBT was virtually identical to the pattern stained by MBP antibody (Figure 3D). These observations indicated that DBT binds specifically to myelin sheaths *in vitro*.

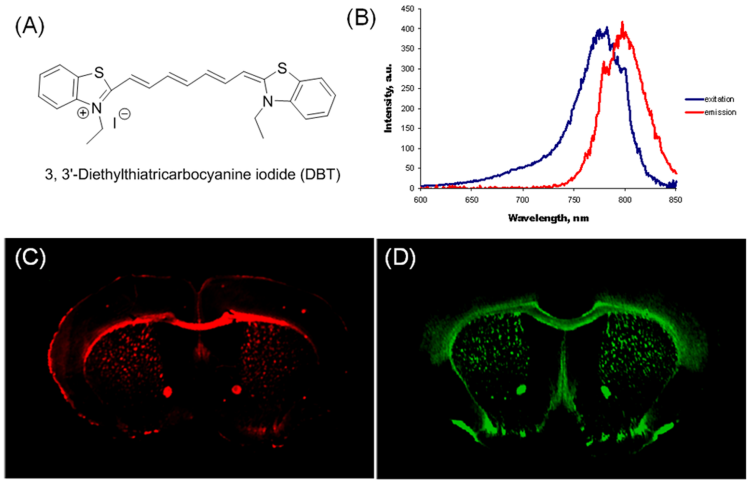

Figure 3. (A) *In vitro* DBT staining of free floating brain tissue sections of wild-type mice (1μM); (B) *In vitro* immunohistochemical staining of free floating brain tissue sections of wild-type mice with MBP antibody. Note that the pattern of labeling is very similar in both cases suggesting that DBT binds to compact myelin

The pattern of binding of DBT and anti- MBP were very similar and competition studies suggest that the binding of DBT blocks the binding of anti-MBP (Figure 4) strongly suggesting that DBT binds directly to MBP.

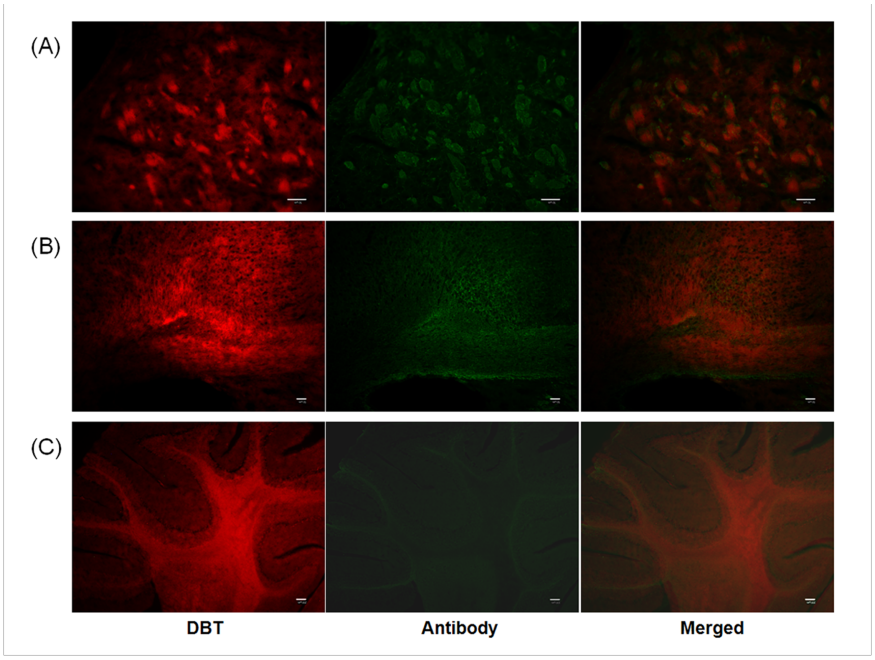

Figure 4. Pre-incubation of frozen sections with DBT blocks the binding of antibodies directed at MBP. A: DBT staining of compact myelin fibers present in caudate putamen significantly blocks anti-MBP binding. B. DBT staining of small myelin fibers present in frontal cortex, significantly blocks anti-MBP binding. C. DBT staining of both myelin tracts and granule layers present in cerebellum, significantly blocks antibody staining of anti- MBP. Scale bar: A, B = 50 µm, C = 200 µm.

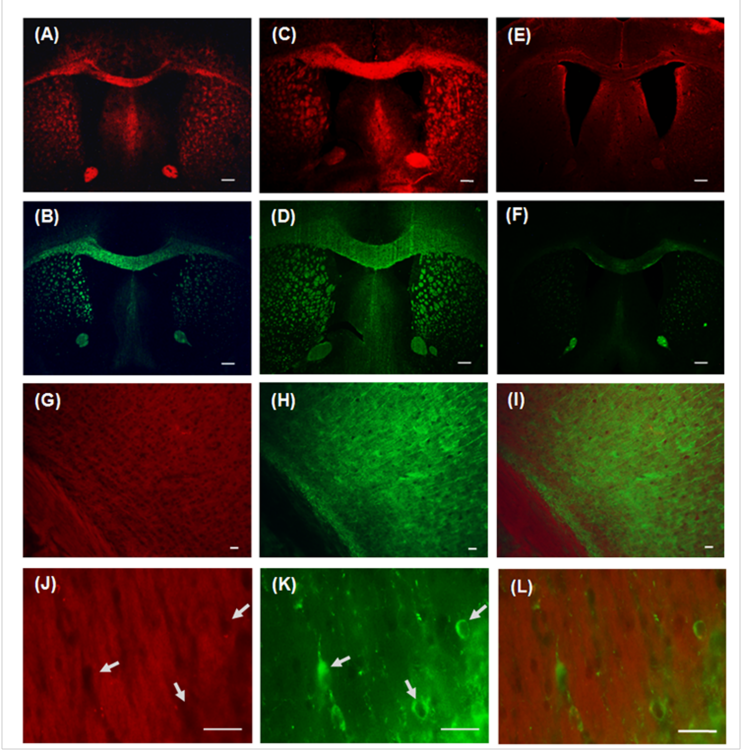

Figure 5. Similar localization and intensity of DBT staining and anti-MBP labeling in sections of wild-type (A, B), hypermyelinated Akt mouse mutant (C, D), and hypomyelinated *shiverer* mouse mutants (E, F). *In vitro* double staining of the corpus callosum and subcortical gray matter using MAP2 antibody (H) and DBT (G) merged (I). Examination of the gray matter at high magnification (40X) to identify subcortical myelinated structures by DBT staining (J) and individual MAP+ neurons (arrows) (K). Lack of DBT binding to neurons highlighted by arrows and merged images in (L). Scale bar: A-F = 300 µm, G-L = 50 µm.

To assess if DBT provided a quantitative assessment of the level of myelination we compared the level of binding in two genetically distinct models. Over expression of the signaling molecule Akt1 in oligodendrocytes results in elevated levels of myelin formation in the CNS, while as discussed above, *shiverer* brains are hypomyelinated. Comparison of the binding of DBT in these genetic models with that in wild type brain sections demonstrated DBT staining of the corpus callosum was significantly higher in the hypermyelinated *Plp-Akt-DD* mouse brain (Figure 5C and 3D) and was significantly reduced in the same region of the *shiverer* mouse brain (Figure 5E and 3F). These studies are consistent with histological studies that have defined the levels of myelination in each of these genetic models. Together these studies suggest that DBT is a good candidate probe for quantitative assessment of the levels of myelination in the intact CNS.

To test whether DBT was capable of crossing the blood brain barrier and providing quantitative data in a longitudinal study of the pattern of detection was undertaken in the same three genotypes using near infrared detection systems. As shown in detail in Dr. Wang's report, DBT effectively crossed the BBB and provided quantitative data on myelin content in a non-invasive manner.

For these studies DBT (0.1 mg/kg) and vehicle (0.05% DMSO/PBS (V/V)) were first administered to the hypermyelinated mouse models through intravenous injections in the tail vein. The fluorescence signals were recorded at 2, 4, 6, 8, 10, 15, 20, 25, 30, 40, 50, 60, 70, 80, 90, 100, 110 and 120 min post-injection. The images recorded at 2, 4, 6, 8, 10, 15, 20, 25, 30 min post-injection are shown in Figure 6 and compared to DMSO/PBS controls. The fluorescent radiance of *Plp-Akt-DD* mice was much stronger than that observed in the wild-type mice, which is consistent with the known increase in myelin content in the *Plp-Akt-DD* mice compared to control animals.

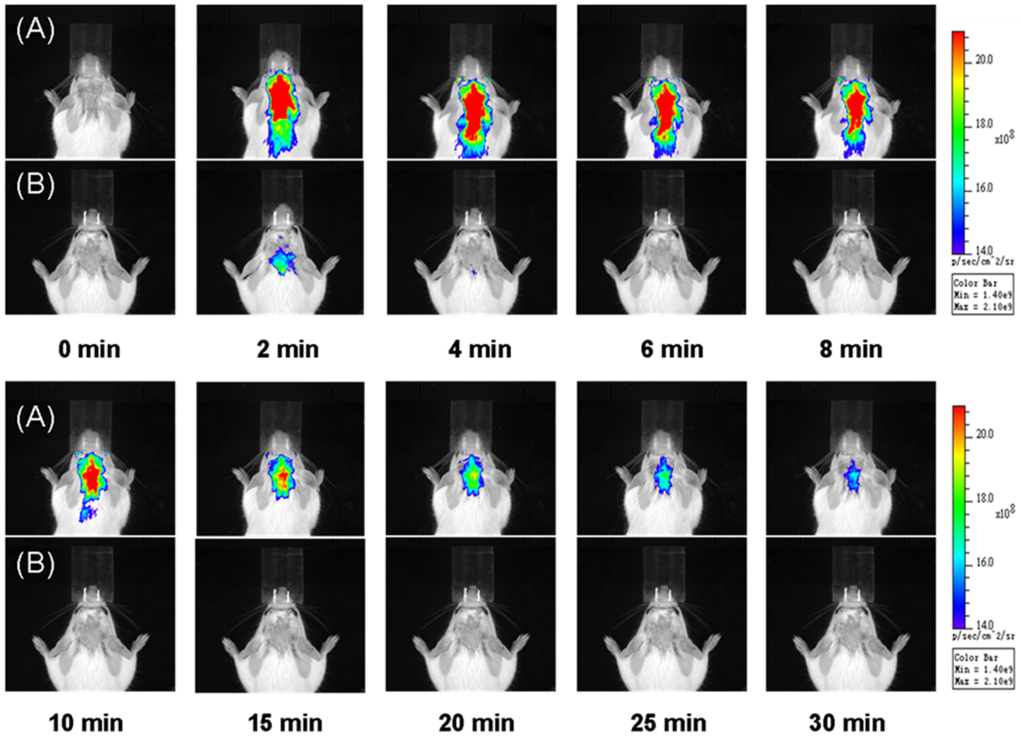

Figure 6. Near-infrared fluorescence *in vivo* imaging in *Plp-Akt-DD* mice (A) and wild-type mice; (B) recorded at 0, 2, 4, 6, 8, 10, 15, 20, 25, 30 min after the i.v. injection of DBT 0.1mg/kg.

Quantitative analyses of these images (Figure 7) demonstrated that over a period of 30 minutes, the average fluorescent intensity of DBT in *Plp-Akt-DD* mice is fourfold higher than that observed in wild-type mice consistent with the enhanced myelin content in *Plp-Akt-DD* mice. The significant difference between the hypermyelinated and wild-type models appeared as early as 2 min post injection with a much stronger fluorescent signal being detected in the hypermyelinated mouse brain, indicating rapid and effective brain entry of DBT in proportion to the myelin content. Compared to the fast clearance of DBT in the WT control, relatively slower clearance was observed in the hypermyelinated mice. These results show the potential of DBT used as a probe for *in vivo* near-infrared fluorescence imaging.

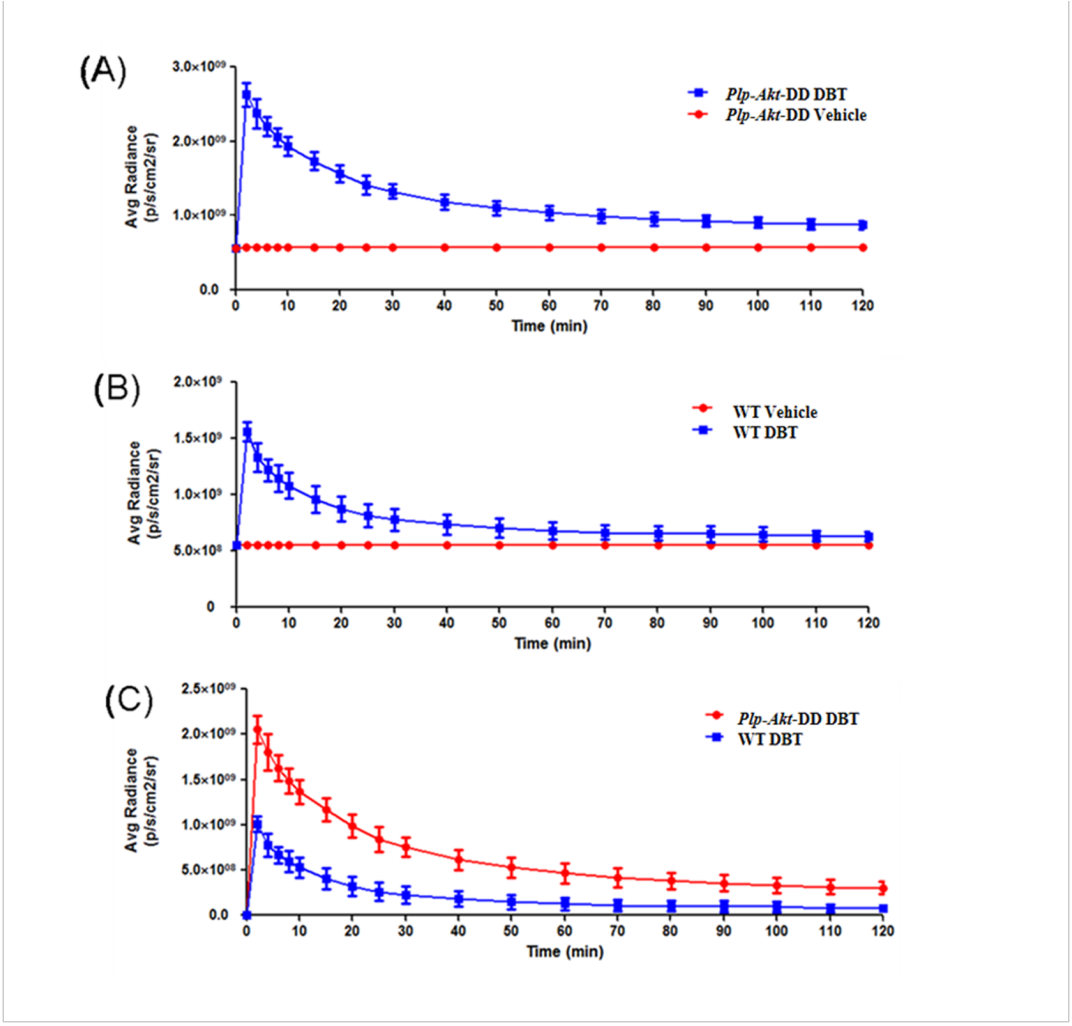

Figure 7. Quantification of *in vivo* imaging of the myelin sheath in living mice. (A) the average radiance of *Plp-Akt-DD* mice after the injection of DBT (blue) and vehicle (red) at 0, 2, 4, 6, 8, 10, 15, 20, 25, 30, 40, 50, 60, 70, 80, 90, 100, 110, 120 min($P<0.0001$, two-tailed t-test, CI 99%). (B) the average radiance of wild-type mice after injection of DBT (blue) and vehicle (red) at 0, 2, 4, 6, 8, 10, 15, 20, 25, 30, 40, 50, 60, 70, 80, 90, 100, 110, 120 min($P<0.0001$, two-tailed t-test, CI 99%). (C) comparison of the average radiance between the *Plp-Akt-DD* mice (red) and wild-type mice (blue) after deducting the vehicle signals ($P=0.0012$, two-tailed t-test, CI 99%). Values are given as mean ±SD.

A similar series of experiments were conducted on the *shiverer* mutant animals. In contrast to the elevated levels of DBT binding seen in the *Plp-Akt-DD* animals, the levels of DBT near infrared single were significantly reduced in the *shiverer* animals compared to controls. Likewise, quantitation of the near infrared signal showed a dramatic reduction in the *shiverer* animals with a greater than 8 fold higher expression in wild type animals. These datum are presented in more detail in the accompanying report by Dr. Wang (see Figures 6 and 7).

While these studies provided important confirmation that DBT binding could identify global changes in myelin expression in genetic models and may therefore be useful in the study of developmental dysmyelinating diseases such as the leukodystrophies, a characteristic of demyelinating diseases in the adult such as Mulitple Sclerosis is that they generate localized pathology. To determine whether DBT could detect pathogenic changes in the levels of myelin expression against a normal background of myelin content, a model of chemically induced demyelination was utilized.

Cuprizone is a cooper-chelating agent that when administered systemically to susceptible animals results in demyelination in the forebrain. The demyelination is largely located in the midline of the corpus callosum although there is some limited involvement of the cerebellum. The spinal cord is largely unaffected in cuprizone treated animals. The time course of the demyelination is protracted. Dosage of the animals for 6 weeks leads to extensive demyelination that can then recover once the toxin is removed. Remyelination takes between 6 and 12 weeks. Using this model we conducted longitudinal NIRF imaging studies at the peak of disease (6th week of treatment) and during remyelination (4th and 8th week of recovery). Fluorescent signals were recorded at 5, 10, 15, 20, 25, 30, 40, 50, 60, 70, 80 and 90 min after i.v. injection of DBT (Figure 8).

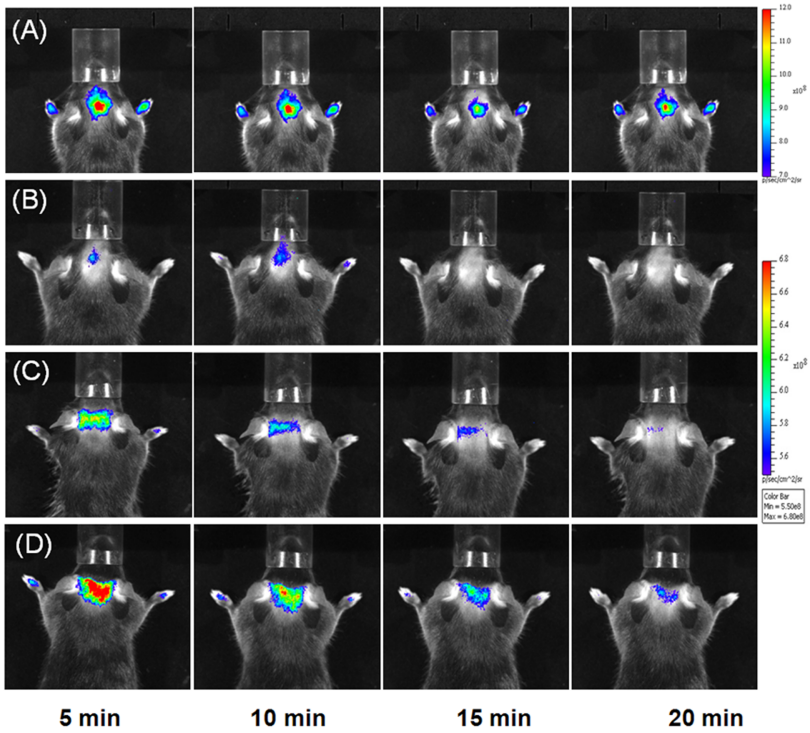

Figure 8. DBT detects demyelination in the cuprizone model of demyelination. (A) near-infrared fluorescence images in a normal control mouse brain (B) mouse brain treated with cuprizone for 6 weeks (C), cuprizone-treated mouse brain after remyelination for 4 weeks (D), cuprizone-treated mouse brain after remyelination for 8 weeks (D). NIRF images of each mouse brain were recorded at 5, 10, 15, 20 min after the i.v. injection of 0.1mg/kg of DBT.

Quantitative image analyses were then conducted to determine the time course of fluorescent radiance detected using the whole brain as region of interest (Figure 9). Compared to wild-type control brains, the fluorescent intensity was significantly reduced in animals following 6 weeks of cuprizone treatments. At 4 weeks of recovery, the fluorescent intensity was increased slightly above the level detected at the peak of demyelination and this was increased further at the 8-week recovery interval. During the course of the study the levels of myelination were assayed by anti-MBP staining on frozen sections from randomly selected animals and the data was consistent with that obtained by imaging (Figure 9).

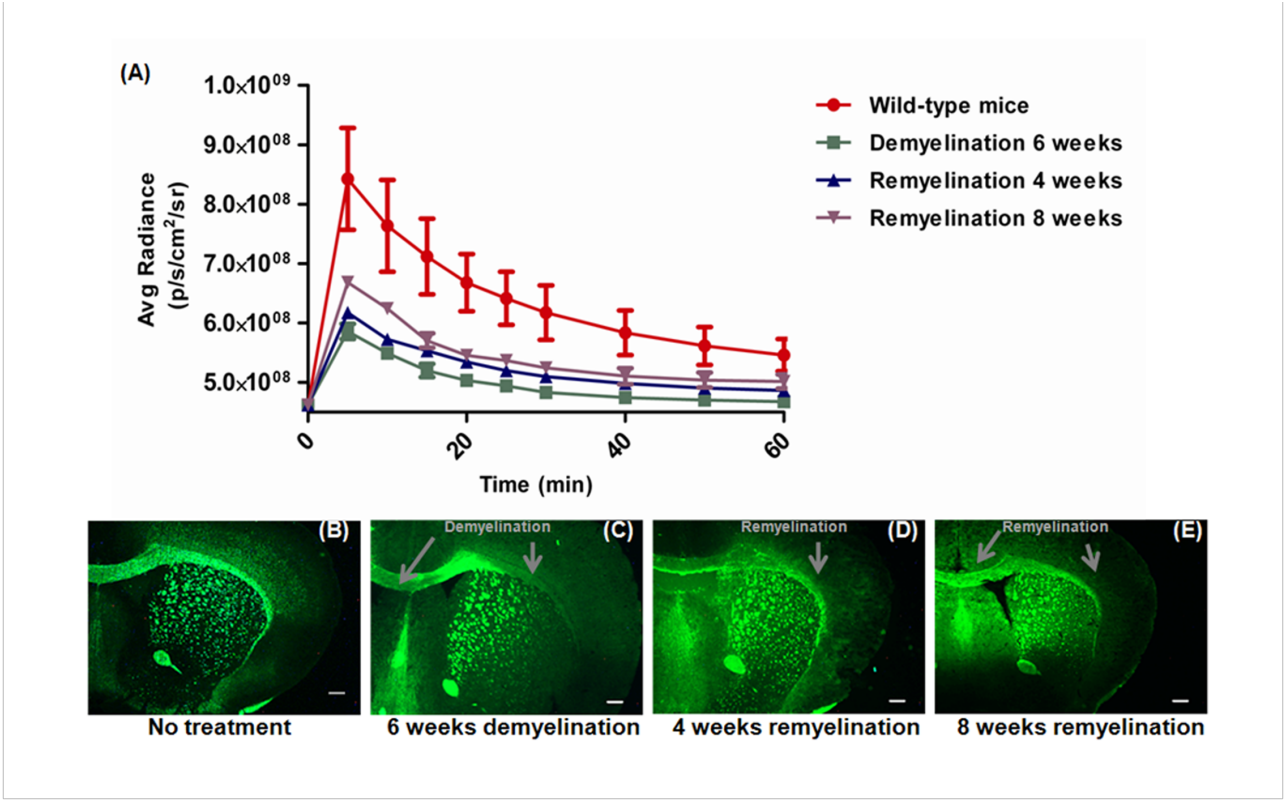

Figure 9. (A) Quantification and comparison of fluorescent intensity in cuprizone induced demyelination and repair. The time courses of the average radiance of DBT detected in normal control mouse brain (red), mouse brain treated with cuprizone for 6 weeks (green), cuprizone-treated mouse brain after remylination for 4 weeks (blue) and cuprizone-treated mouse brain after remylination for 8 weeks (purple) (P=0.0006, one-way ANOVA test, CI 95%). Value are given as mean ±SD; (B-E) After imaging anti-MBP labeling was conducted at different stages including control (B), cuprizone-induced demyelination (C), remyelination at 4 weeks (D), and remyelination at 8 weeks (E). Scale bar: 300 μm

These studies indicate the capacity of DBT to identify wide spread demyelination induced by cuprizone toxicity in the forebrain of susceptible animals. The pathology of MS, and the majority of the lesions that result in functional deficits, are however more prominent in the spinal cord rather than forebrain. To determine whether probes developed by Dr. Wang were

capable of detecting lesions within the spinal cord, we utilized an alternative probe termed MeDAS.

3. Use of MeDAS to follow remyelination in the intact CNS in response to potential therapy treatments.

The ultimate goal of this project is to develop probes that can be used to non-invasively determine the levels of myelination in specific regions of the CNS in the living subject and to determine if potential therapies that result in functional benefit are generating functional improvement as a consequence of myelin repair rather than immunological suppression. To generate a comprehensive data set that included the therapy treatment we selected to utilize the fluorescent probe termed Me DAS that was generated by Dr. Wang during the course of the project.

These studies involved many of the approaches used in analysis of the probes discussed earlier in the report as well an additional set of animal models that involved survival surgery. All animal surgery and care was performed in accordance with the Institutional Animal Care and Use Committee of Case Western Reserve University. The models are outlined below.

3.1.a. Induction of focal demyelination in the spinal cord

A model of choice for the analyses of therapies that promote myelin repair in the adult CNS is the focal demyelination lesion model that develops as a result of the localized injection of a gliotoxin such as LPC into defined regions of the brain and spinal cord. This model has a number of advantages for characterization of imaging modalities and assessment of the efficacy of therapy treatment in myelin repair. For example, the lesion is accurately defined in time and space, the rate of endogenous repair is well established and the histological assessment of remyelination is unambiguous. In this model, LPC was directly injected into the spinal cord of Sprague-Dawley (SD) female rats (8-10 weeks old, 220-240 g) as previously described (Kerstetter et al., 2009). Animals were anesthetized using a mixture of rodent cocktail. For post-operative pain relief, Torbugesic (2 mg/kg) was subcutaneously administered prior to surgical procedure. A T10 laminectomy was performed by first making lateral longitudinal incisions in the paraspinal muscles from the middle of T-11 through the middle of T-12. A beveled microcapillary glass needle attached through small diameter tubing to a microinjection system (using a 10 µl Hamilton syringe) was then directed 1 mm into the dorsal column of the spinal cord with the aid of a Stoelting stereotaxic manipulator. LPC was injected into the dorsal column in a dose of 1.5 µl at 1% concentration, at a rate 0.25 µl/min. The needle was left in place for up to 5min before removal to ensure there was no backflow of the solution. The animals were allowed to recover in a clean cage on a heating pad and treated with analgesics as needed.

3.1.b. Induction of EAE in Lewis rats

While the LPC model is excellent for quantifying the rate of remyelination in the presence or absence of therapeutic intervention, it lack the long term engagement of the immune system that is a characteristic of MS. Thus, we selected to use an alternative model of experimental allergic encephalitis (EAE) and disease progression was tracked through MeDAS binding. Two sets of 8-week old female rats, 3 Lewis Rats and 3 Sprague Dawley rats were purchased from Charles River Laboratories, in Wilmington MA and maintained in the animal resource center for one week after arrival. Animals were immunized with a emulsion of recombinant Myelin Oligodendrocyte Glycoprotein (rMOG 1-125, from Biogen Idec.), freshly prepared by

initially diluting rMOG in 0.01M phosphate buffered saline (PBS, pH 7.4) to a final concentration of 2 mg/ml. Equal volumes of MOG/PBS and Complete Freund's Adjuvant were mixed thoroughly (CFA (2mg/ml), Chondrex, Inc, WA), the emulsion gently centrifuged, and loaded slowly into a 1-ml syringe for subcutaneous injection. Rats were anesthetized with rodent cocktail before emulsion injections, and administered 100 µl of inoculum by intradermal injection at the base of the tail. Each rat received 50 µg of rMOG 1-125. Animals were assessed for progression of disease after immunization, weighed and scored daily for signs of EAE according to the following scale: 0, no disease; 1, tail paralysis; 2, hind limb weakness; 3, hind limb paralysis; 4, hind limb paralysis and forelimb weakness; 5, moribund or dead.

3.1.c. Induction of neuroinflammation through delivery of lipopolysaccharide (LPS)

To determine whether the imaging approaches could distinguish between demyelination and inflammation in the CNS, a model of CNS inflammation was developed. Female SD rats (n=3, 6-8 weeks of age) were anesthetized with rodent cocktail and positioned in a stereotaxic frame (Stoelting). The scalp was incised and retracted so the cortex and corpus callosum could be targeted using the following stereotaxic coordinates: (relative to bregma) anterior–posterior (AP), 3.0 mm; medial–lateral (ML), 1.0mm; and dorsal–ventral (DV), 2.0 mm for cortex, and AP, 0.0 mm; ML, 2.0mm; and DV, 4.5 mm for corpus callosum. Two small holes were drilled in the skull, and a 33S gauge needle attached to a 10 µL Hamilton Syringe was lowered into the cortex and corpus callosum guided by the above coordinates. A mini injector pump (Stoelting) controlled the infusion of 3 µL of LPS (E. coli, serotype 055:B5, 1mg/ml) at a rate of 0.25 µL/min, after which the needle was left in place for 2 min to prevent liquid reflux out of the brain parenchyma. The incision was then closed, and the animals were allowed to recover on a heating pad.

3.1.d. Histopathology

To validate the microPet studies, the same animals were subsequently sacrificed and used for histo-pathological analysis. The animals were sacrificed by a transcardial perfusion of saline followed by 4% polyformaldehyde (PFA) under terminal anesthesia. The spinal cord and brain were carefully removed and postfixed in 4% PFA overnight, followed by infusion with 10%, 20% and 30% sucrose solutions. Selected areas were sectioned at 20µm on a cryostat, and mounted directly onto Superfrost Plus microscope slides. The slides were then subject to either staining to detect neuroinflammation or Black Gold, Luxol Fast Blueor MeDa staining to detect myelin as previously described (Mi et al., 2007; Wu et al., 2008; Wang et al., 2009).

3.1.e. Detection of Neuroinflammation

Following cryoprotection in graded sucrose and rapid freezing, 20uM serial sections through regions of interest were prepared on a Microm HM525 cryostat. The sections were air-dried and kept at -20^{o}C until labeling. To detect neuroinflammation selected sections were brought to room temperature allowed to air-dry and rehydrated in PBS. The PBS was removed, and the sections blocked with 5-10% Normal Goat Serum in 0.1% Triton-X 100 in PBS for one hour at room temperature to reduce non-specific staining. The antibodies, IBA1 (Rabbit polyclonal, Wako Cat. #019-19741) or GFAP (Rabbit polyclonal, Dako Z0334), were diluted 1:500 in blocking medium containing 5% NGS, and the sections incubated overnight at 4^{o}C. The following day, the sections were rinsed, incubated 1.5 hours in the secondary antibody (Invitrogen goat anti-Rabbit IgG Alexa-594), washed thoroughly and mounted in Vectashield. Sections were imaged on a Leica DM 5500B microscope and the images recorded using a Leica DFC 500 camera.

3.1.f. Ex vivo fluorescent tissue staining of myelin

To detect the labeling of myelin specific probes in sections of the CNS a dose of (25 mg/kg) of MeDAS was administered via tail-vein injection to a Female SD rat. At 2 hours post-injection, the rat was deeply anesthetized and perfused transcardially with saline and 4% paraformaldehyde (PFA) as described above. The brain and spinal cord were removed and postfixed by immersion in 4% PFA overnight, infused with 30% sucrose and embedded in the mounting compound OCT (Fisher Scientific, Suwanee, GA). Samples were sectioned at 20 µm on a microtome, and sections mounted on superfrost slides (Fisher Scientific) with fluoromount-G mounting media (Vector Laboratories, Burlingame, CA). Due to the fact that MeDAS is inherently fluorescent, the binding to white matter regions rich in myelin was directly detectable using a Leica DRMB microscope equipped for fluorescence.

3.1.g. HFG treatment

One major goal of this program is to determine whether one can use longitudinal imaging to assess the efficacy of therapeutic approaches to myelin repair. The selected therapy for these studies was hepatocyte growth factor (HGF), which we recently demonstrated was one of the primary components of mesenchymal stem cell conditioned medium responsible for myelin repair (Bai et al., 2012). In these studies an LPC lesion was induced as described above, and the animals were treated with 2 doses of HGF systemically. Because there is an initial immunological response to the demyelinating lesion, delivery of the first dose was delayed for 4 days after lesion induction. Animals were randomly assigned to either control (saline, n=6) or experimental (HGF treatment, n=8) groups. The experimental group received 0.4 and 0.8µg/Kg of HGF via tail vein injection on days 4, 6, and 12 post lesion. The controls received an equivalent volume of saline, and the animals were imaged on days 7, 14, and 21 post LPC treatment. At the termination of the study the animals were sacrificed and the level of myelin repair in the lesion compared between control and experimental animals.

3.1.h. MicroPET/CT imaging of spinal cord and data acquisition

PET imaging of [^{11}C]MeDAS was performed using a Siemens Inveon microPET/CT scanner in the Case Center for Imaging Research. For better anatomic localization, CT co-registration was applied. For LPC treated rats, PET/CT scans were performed on days 0, 7, 14, and 21, following LPC injections in spinal cord. For EAE rats, PET scans were performed on day 0, and the first, second, and third disease episodes after MOG induction. The rats were fasted overnight prior to imaging, but had access to water. Their diet was replenished after imaging. Before PET imaging, CT scout view was taken to ensure most of the vertebrae, especially the ilium, were placed in the co-scan field of view (FOV) where the highest image resolution and sensitivity is achieved. Approximately 37 MBq of [^{11}C]MeDAS was injected through the tail vein, and dynamic microPET data acquisition was performed in a list mode immediately. During the scans, body temperature of the anesthetized rats was maintained at 34+/-2°C with a heating lamp. Once the dynamic acquisition was done, a CT acquisition scan was performed for attenuation correction.

3.1.i. Quantitative image analysis

Quantitative image analysis of the uptake of [^{11}C]MeDAS in spinal cord was performed using Carimas II software. This program allows an ROI to be extrapolated from the reconstructed microPET image frames in order to determine the SUV in a specific region. Based on the PET and CT co-registered images, the rat's ilium was used as a marker to accurately identify

vertebrae. For LPC treated rats, lesion vertebrae (Thoracic 11 and Thoracic12) were then defined as the regions of interest (ROI). For EAE rats, every single rat vertebrae (from Thoracic 8 to Lumbar 1) was defined as a ROI. The radioactivity data were decay-corrected and normalized by the body weight of the rats, and amount of [^{11}C]MeDAS injected. Radioactivity concentration in the spinal cord is expressed in terms of standard uptake value (SUV) [(μCi/cc)/(uCi/g)] as a function of time. The time activity curve (TAC) for each vertebra was obtained.

3.1.j. MicroPET imaging in acute neuroinflammation rat model and data acquisition

Following the induction of CNS inflammation, rats were placed in an Inveon microPET scanner under anesthesia. After a 10 min transmission scan with a Co-57 source, 37 MBq of [^{11}C]MeDAS was administered via tail vein injection, and immediately followed by a dynamic acquisition of up to 90 min. A two-dimensional OSEM algorithm was used for image reconstruction. Decay, attenuation, and scatter correction were all performed during the image histogram and reconstruction processes. For better anatomic localization, a MRI scan was also performed. After microPET imaging, the same bed was transferred to a MRI scanner (Bruker Biospin 7.0T, Billerica, MA). The rat's head was well positioned in the center of the rat coil. A rapid-acquisition relaxation-enhanced (RARE) analysis (TR/TE = 2000/40 ms, 4 echoes, FOV = 45 mm × 45 mm, matrix = 256 × 256) was used to acquire 15 contiguous 1 mm axial images of each animal's brain. Co-registration of MRI and PET images was conducted using the MATLAB-based program Compartmental Model Kinetic Analysis Tool (COMKAT). For quantitative image analysis, the whole brain was considered as a ROI, and was defined based on the co-registered images to measure the radioactivity concentration in the whole brain. The radioactivity data was decay corrected and normalized by the body weight of the rats, and amount of [^{11}C]MeDAS injected.

3.1.k. Statistical analysis

In this study, all data is expressed as a mean ±SD. A Student's t test was used to evaluate if there is any significant difference between each groups of studies. A p value of <0.05 was accepted as significant.

3.2.a. In vitro tissue staining of the spinal cord

MeDAS is a fluorescent compound with maximum excitation and emission wavelengths of 363 and 419 nm, respectively (Wu et al., 2008). So the myelin binding property of MeDAS can be evaluated based directly on fluorescent microscopy. In a first set of studies, section of rat spinal cord were directly incubated in a solution of MeDAS in 10% DMSO. For this purpose, a series of axial sections of the spinal cord were prepared so that both myelin-rich white matter and myelin-deficient gray matter could be visualized. To determine whether MeDAS could accurately identify changes in the normal pattern of myelination, the distribution of labeling i was compared in sections taken from wild type control animals as well as from animals that had previously received either an LPC demyelinating lesion or had ongoing EAE. To validate MeDAS staining the pattern of binding was correlated with that seen with Black-Gold staining, on adjacent sections. At a 10μM concentration, MeDAS selectively stained the spinal cord white matter and significantly lower levels of MeDas labeling were seen in the central gray matter of the spinal cord. This differential distribution is consistent with the pattern of labeling seen with black gold staining and reflects the differential levels of myelin in white and gray matter in the spinal cord (Figures 10A and 1B).

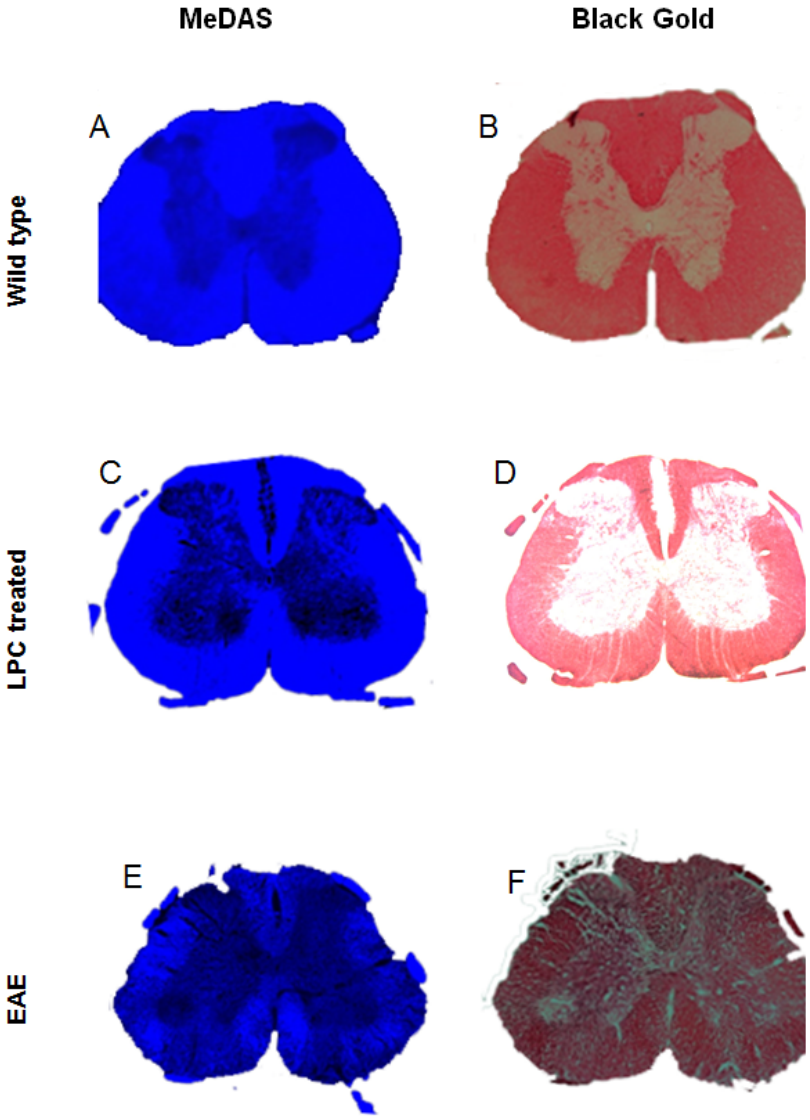

Figure 10. *In vitro* MeDAS staining of the spinal cord tissue sections from wild-type, LPC-treated and EAE rats that are consistent with Black-Gold staining in adjacent tissue sections.

The staining of MeDAS correlates directly with the presence of myelin sheaths. In the models of demyelination, the localized loss of myelin sheaths resulted in a significant disruption in the binding of MeDAS. This was observed in fluorescent MeDAS staining of the spinal cord, with focal demyelination in the white matter that was induced by stereotactic injection of LPC. Our previous studies have shown that LPC treatment led to focal myelin loss with significant sparing of other cell types, such as axons and astrocytes (Wang et al., 2009). As shown in Figure 10C and 1D, the demyelinated foci in the dorsal columns of the spinal cord are readily visualized by MeDAS fluorescence, and provide a image that was identical to Black-Gold staining on adjacent sections. Thus, MeDAS is capable of detecting demyelinated lesions. Similarly, in the spinal cord of EAE rats where the regions of demyelination are less reproducible but often located at the periphery of the spinal cord, MeDAS staining showed profound demyelination across the peripheral white matter in parts of the most affected vertebrae, as confirmed by the Black-Gold staining (Figure 1E and 1F). These data provide strong support of the notion that MeDAS is selectively binding to myelin sheaths and that the level of binding can distinguish areas of myelin perturbation.

3.2.b. In situ detection of myelin in rat brain and the spinal cord

Following *in vitro* tissue staining, we investigated the ability of MeDAS to stain myelin tracts *in situ*. In these studies a single dose of MeDAS (20 mg/kg) was administered to wild-type SD rats via tail vein injection. Two hours later, upon perfusion, the brain and the spinal cord were

then removed and sectioned, and the fluorescent MeDAS distribution was directly examined under fluorescent microscopy. As shown in Figure 11, the myelinated corpus callosum and the white matter of spinal cord are clearly visualized by MeDAS staining with fluorescent patterns that were consistent with Black-Gold staining in adjacent sections. These studies suggested that MeDAS readily entered the brain and spinal cord and selectively labeled the respective myelinated regions in the white matter.

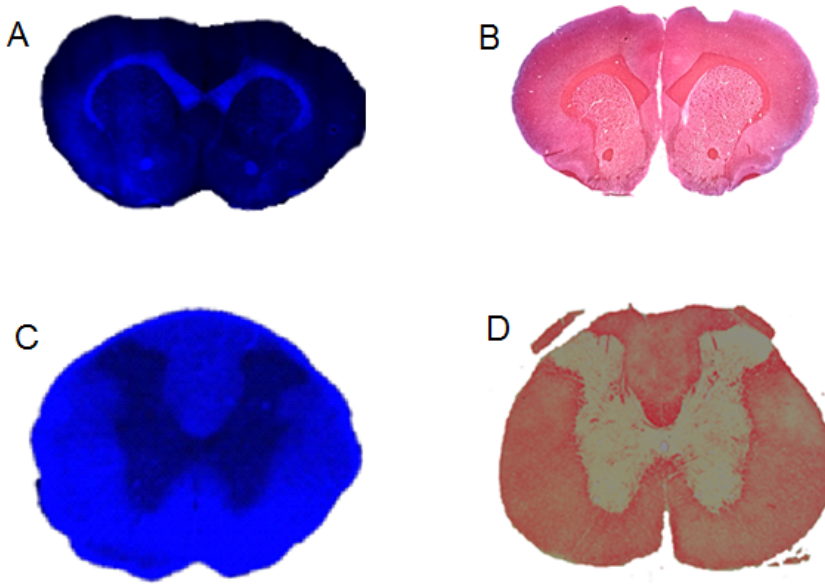

Figure 11. *In situ* MeDAS staining of myelin sheaths in the brain (A) and spinal cord (C) two hours after single dose (20 mg/kg) administration via tail vein injection, which correlates with Black-Gold staining in adjacent tissue sections (B and D, respectively).

These studies provided confidence that the imaging probe had the characteristics suitable to allow the longitudinal analyses of myelin repair in animal models of MS. The Wang group 9 then undertook a series of studies to examine biodistribution and in vivo competition studies using earlier developed probes (Wang et al., 2010). These data are outlined in detail in his report, but briefly showed that MeDAS rapidly passed through the blood-brain barrier and its retention was higher in neural tissue than any other tissue, although some residual binding was seen in bone and adrenals. In a series of competitive binding studies using a previously developed myelin-binding agent (BMB), as a blocking agent, which has shown high affinity for myelin (Stankoff et al., 2006) they showed that when the rats were pretreated with BMB (10 mg/kg) at 3 hrs prior to [^{11}C]MeDAS-PET imaging, the specific binding was significantly reduced. At 40 min post-injection, for example, the specific binding to myelin rich areas in pretreated compared to control rats was reduced by approximately 50% in all the regions.

3.2.c. Effects of neuroinflammation on PET imaging of demyelination

One challenge to developing an imaging probe for a demyelinating disease such as MS is that it has to be able to distinguish between frank demyelination and neuroinflammation. Frequently, both are present in MS lesions and while it is critical to regulate CNS inflammation understanding the targets of pharmacological or cellular therapies require that the imaging probe is capable of distinguishing between the two pathologies. To determine if neuroinflammation has any effects on [^{11}C]MeDAS uptake, we prepared an acute neuroinflammation model by stereotaxic injection of LPS to the rat brain (Wenk et al., 2004). Subsequent histological analysis showed that one day after injection, profound inflammation developed in the rat brain while myelin sheaths remained intact. Neuroinflammation is characterized by increased activation of microglial cells, the macrophage equivalent in the

brain and spinal cord as well as an activation of astrocytes. Microglial cells can be identified through the expression of IBA1 and antibodies to IBA1 selectively bind to microglia. The reaction of astrocytes to neuroinflammation is complex and results in both hypertrophy and occasionally proliferation. One characteristic change of reactive astrocytes is significant upregulation of the expression of the intermediate filament protein glial fibrillary acid protein (GFAP). Following LPS injection immunohistology showed profound microglia activation and macrophages in the brain by IBA1 staining (Figure 12A and 3E). Reactive astrocytes were also detected by GFAP staining (Figure 12B and 3F). In the meantime, the myelin integrity remained intact as demonstrated by Luxol Fast Blue staining (Figure 13C and 4G), and *in vitro* MeDAS staining (Figure 12D and 3H). Using this neuroinflammation rat model, we conducted PET studies to determine [^{11}C]MeDAS uptake before and after the inflammation was induced and to assess the effects of inflammation on that uptake. As shown in Figure 12 I and 3J, [^{11}C]MeDAS uptake was practically identical before and after LPS treatment. Thus, induction of inflammation did not alter the pharmacokinetics of [^{11}C]MeDAS in the brain.
These studies suggested that [^{11}C]MeDAS-PET is a specific imaging marker of demyelination, and that this is not significantly altered by coincident neuroinflammation.

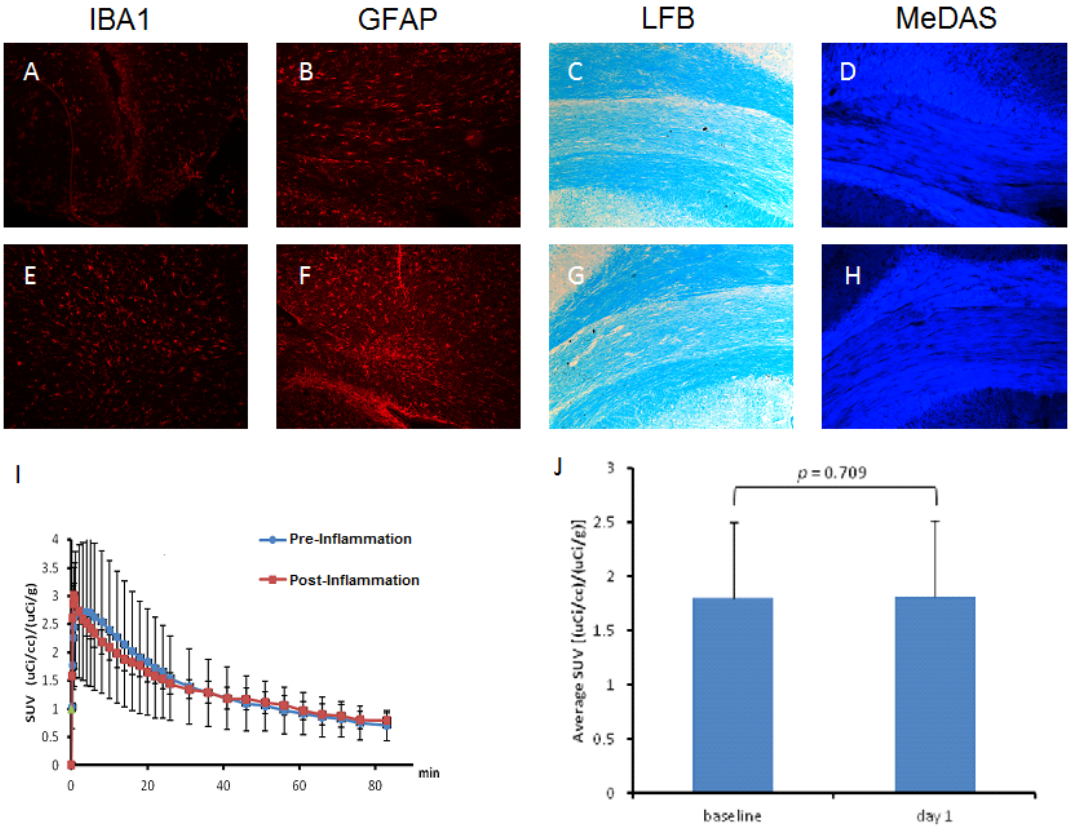

Figure 12. Immunohistochemical staining and [^{11}C]MeDAS-PET studies in the rat brain at 24 hours after induction of neuroinflammation by LPS. A-D: Immunohistochemical staining of the right hemisphere of the rat brain including IBA1 staining of activated microglia and macrophages (A), GFAP staining of astrocytes in reactive form (B), Luxol Fast Blue and MeDAS staining of intact myelin tract (C and D). E-H: the corresponding staining results in the left hemisphere. I. [^{11}C]MeDAS uptake as a function of time over the 90 min scan showing

similar pharmacokinetic profiles before and after induction of inflammation. J. Average brain uptake of [^{11}C]MeDAS over the 90 min of PET scan suggesting that neuroinflammation has no effects on [^{11}C]MeDAS uptake.

3.2.d. Longitudinal PET imaging of the spinal cord in a LPC rat model

We then evaluated the ability of [^{11}C]MeDAS-PET to longitudinally assess myelin content in the spinal cord *in vivo*. To quantitatively characterize demyelination and remyelination, we first induced a focal demyelinated lesion (T11-12) by stereotactic injection of LPC to the spinal cord. The rat was then subjected to a serial PET/CT imaging at the peak of demyelination (7 days post injection), and during the course of remyelination (14 and 21 days post injection). As shown in Figure 13A, the rat spinal cord was readily visualized by [^{11}C]MeDAS-PET with high specificity and sensitivity. The uptake of [^{11}C]MeDAS in the affected region of the spinal cord at various time points was quantified. As shown in Figure 14B, [^{11}C]MeDAS uptake was lowest at day 7 when demyelination was peaked. At day 14 and day 21 post injection, [^{11}C]MeDAS uptake gradually increased due to the process of remyelination.

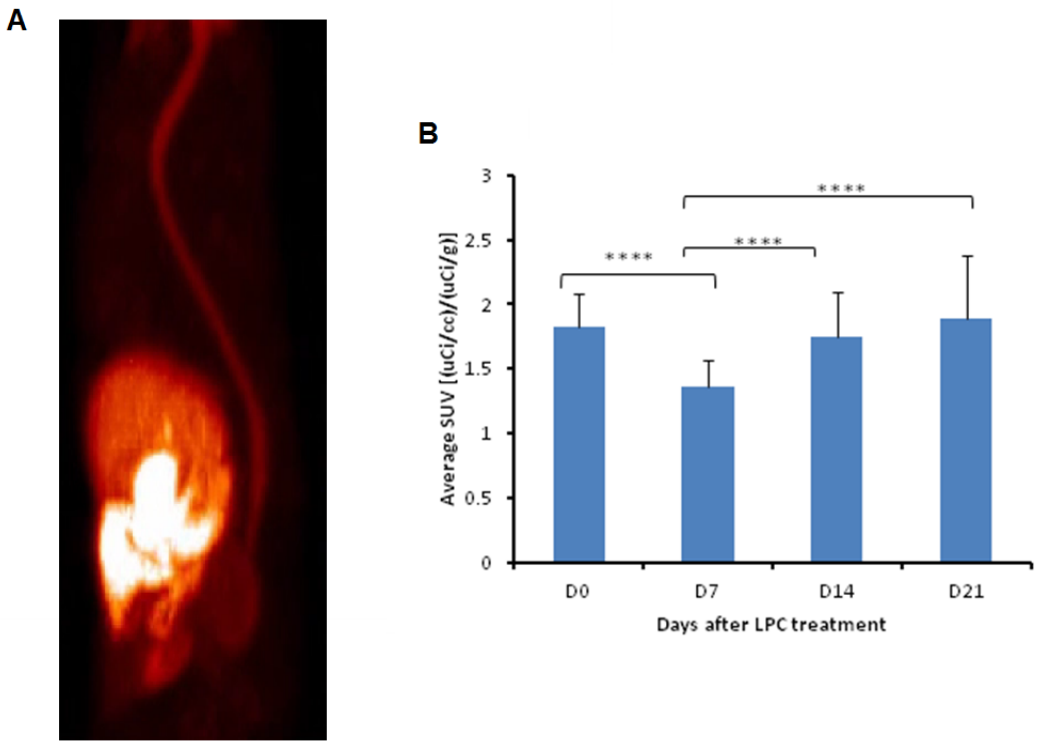

Figure 13. A: representitative PET image of the rat spinal cord. B: Longitudinal PET studies in the LPC-treated rats over 21 days. The average uptake in the spinal cord (T11-12) was quantified on day 0, 7, 14, and 21. On day 7 of demyelination, the uptake of [^{11}C]MeDAS in the T11-T12 region decreased by 34% compared to day 0. On day 14 and 21 of remyelination, the uptake of [^{11}C]MeDAS in the T11-T12 region increased by 22% and 28%, respectively, compared to day 7.

The level of remyelinaiton was confirmed using toludine blue labeled epon sections and representative samples are shown in Figure 14.

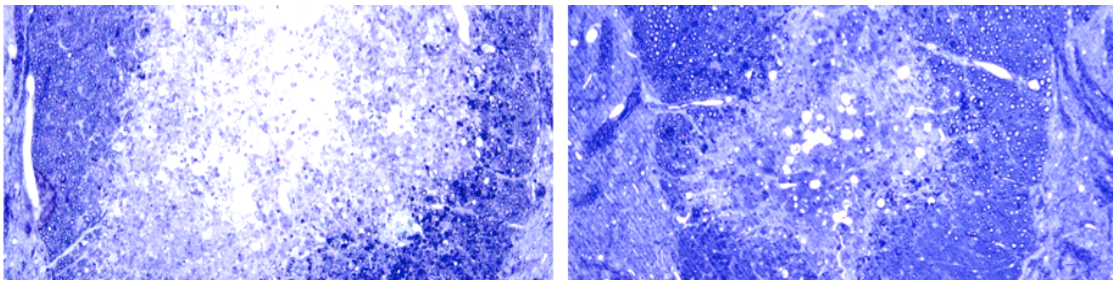

I week post LPC 3 weeks post LPC

Figure 14. At one week post PLC lesions the lesion area is significantly reduced in the level of myelin and the number of myelinated axons as shown by the relatively light level of toluidine blue staining. By contrast, at 3 weeks post LPC while the level of myelination as not returned to pre-lesion levels it is significantly higher than at earlier post lesion times.

3.2.e. Longitudinal PET imaging of the spinal cord in EAE rat model

While the LPC model represents pure demyelination/remyelination, EAE is an animal model that closely mimics the MS pathology because it incorporates immunological induction of neuropathology. We therefeore conducted a series of [^{11}C]MeDAS-PET imaging in an EAE rat model to longitudinally monitor myelination in the spinal cord. In this study, EAE was induced by immunizing 3 SD rats and 3 Lewis rats with MOG1-125 peptide. Starting at day 7 after immunization, the SD and Lewis rats developed paralysis of hind limbs, with an EAE score reaching 3.0 or above in a relapsing and remitting pattern. In this study longitudinal PET imaging was conducted at three time remitting points of the disease and [^{11}C]MeDAS uptake in different vertebrae regions was quantified. In the EAE SD rats, [^{11}C]MeDAS was not evenly distributed across the spinal cord. Before immunization, [^{11}C]MeDAS uptake was relatively high in part of the thoracic region (T10-T13) (Figure 15A). After immunization, [^{11}C]MeDAS uptake was significantly decreased across the whole spinal cord, particularly between thoracic regions T10-T13 (Figure 15B). The average [^{11}C]MeDAS uptake was determined from L3 to T8 at the three episodes on days 15, 25, and 42 (Figure 15C). Compared to pre-immunization, the average [^{11}C]MeDAS uptake decreased significantly at all three episodes (Figure 15C). Particularly at the third episode on day 42 when the EAE score was almost 5.0, [^{11}C]MeDAS uptake reached the lowest level (Figure 15D). The greatest change was observed in the region between T10-T13 as shown in the representative PET and CT fusion image of the spinal cord in the SD rat on day 42 after immunization with MOG1-125, which was reconstructed based on uptake of [^{11}C]MeDAS (Figure 16). These data suggest that the pattern of demyelination is variable along the length of the spinal cord and that the level of pathology is variable over time. Such observations are entirely consistent with previous histological studies in this model.

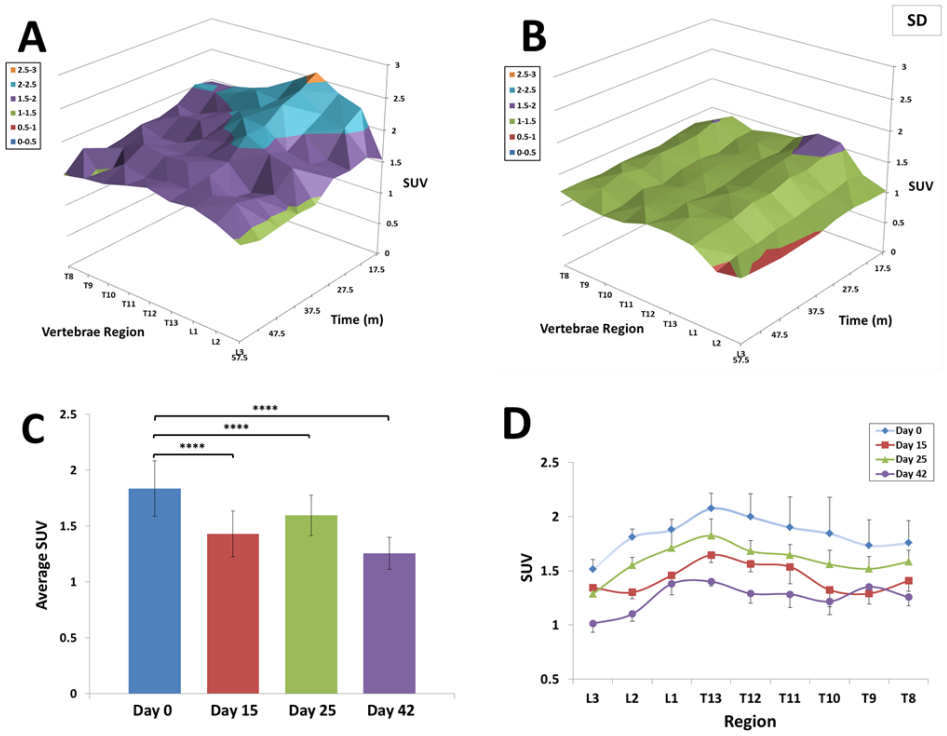

Figure 15. A: [^{11}C]MeDAS uptake across regions L3-T8 from 17.5 min to 57.5 min of a control SD rat. B: [^{11}C]MeDAS uptake across regions L3-T8 from 17.5 min to 57.5 min of an EAE SD rat after immunization with MOG1-125. Note homogenous demyelination in these regions, characterized by a lower SUV. C: Average SUV values over the L3-T8 region in the SD rat on day 0, 15, 25, and 42. D: Average SUV values by spinal region in SD rat for each scan. Note the most premilent changes occur in the L3-T8 region. Error bars refer to absolute error.

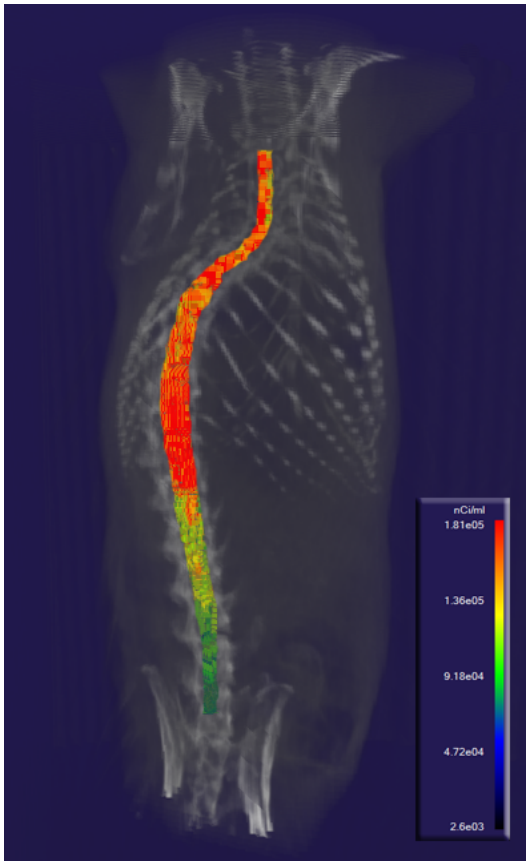

Figure 16. Three-dimentional PET and CT fusion image of the spinal cord in a SD rat on day 42 after immunization with MOG1-125.

In the EAE Lewis rats, similar pattern of [^{11}C]MeDAS distribution was observed. Before immunization, [^{11}C]MeDAS uptake was relatively high in the thoracic region between T9-T13 (Figure 17A). After immunization, [^{11}C]MeDAS uptake decreased significantly in the lumbar regions (L1-L6) compared to other regions in the spinal cord (Figure 17B). The average [^{11}C]MeDAS uptake was then determined at the three peaks of the disease: on days 26, 33, and 39 (Figure 17C). This is particularly apparent at the third episode when the EAE symptoms were most severe. Unlike the EAE SD rats, the EAE Lewis rats showed the most difference in the lumbar region between L1 and L6 (Figure 17D). Post-mortem histochemical staining using both MeDAS and Black-Gold displayed significantly low fluorescence in the white matter of the spinal cord (Figure 11E and 11F).

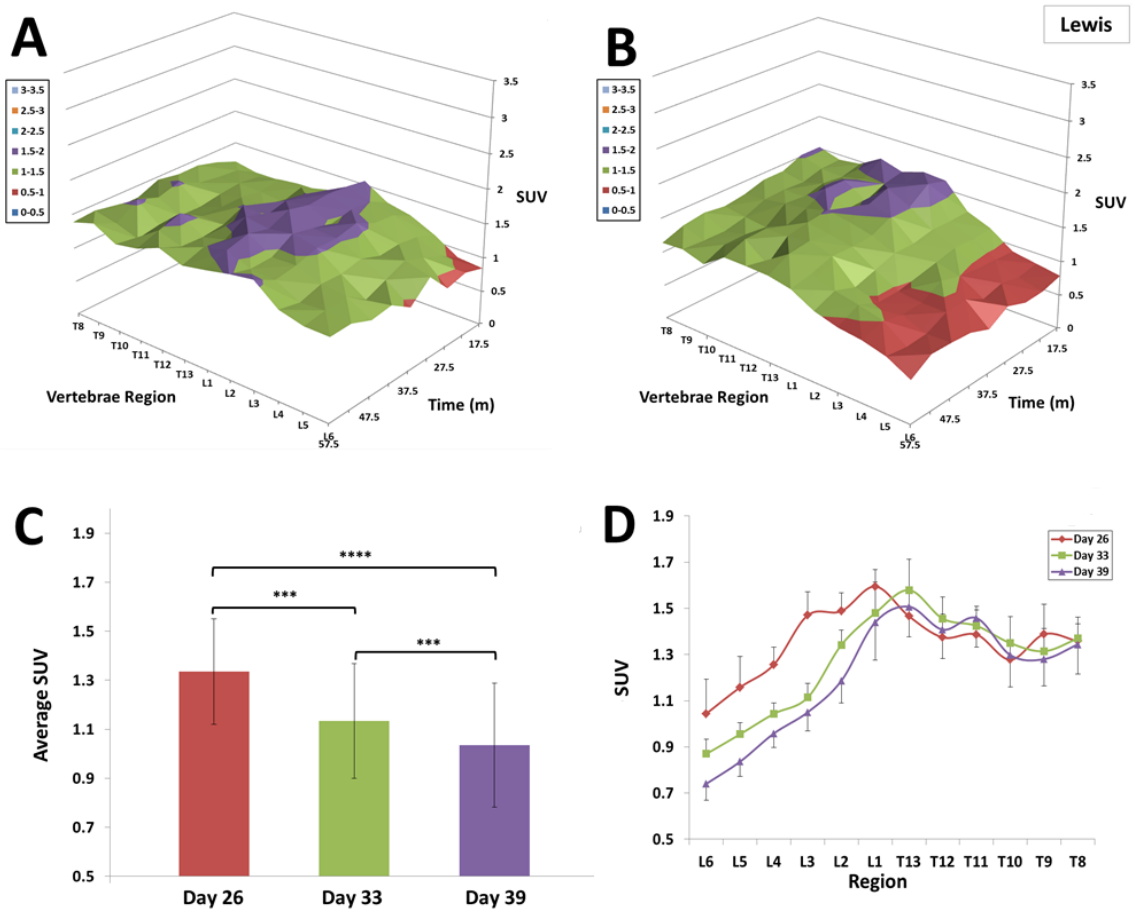

Figure 17. A: [^{11}C]MeDAS uptake across regions L6-T8 from 17.5 min to 57.5 min of a control Lewis rat. B: [^{11}C]MeDAS uptake across regions L6-T8 from 17.5m to 57.5m of an EAE Lewis rat. Note significant demyelination in the Lumbar vertebrae, characterized by a lower SUV in these areas. C: Average SUV values over the L6-L1 region in the EAE Lewis rat on day 26, 33, and 39 after immunization of MOG1-125. D: Average SUV values in the L6-T8 region in the EAE Lewis rat for each.

The Wang group then went on to characterize the detection limits of demyelination and remyelination and assess the different factors that contribute to the limits of detection of demyelination and remyelination (Wang et al., 2011).

A key challenge in the development of therapies that promote myelin repair in the CNS is identifying the effectiveness of the treatment in longitudinal studies. The development of the imaging probes by Dr. Wang provides a unique opportunity to assess myelin repair in a non-invasive manner. To provide proof of principle data we selected to assess the capacity of MeDAS to report myelin repair in response to hepatocyte growth factor stimulation.
In previous studies we have demonstrated that the functional recovery that is seen following treatment of demyelinated animals with mesenchymal stem cells is dependent on their release of hepatocyte growth factor (Figure 18) (Bai et al., 2012).

Figure 18. Hepatocyte growth factor is present in MSC conditioned medium and enhances functional recovery in EAE. Ultrastructural analysis demonstrates that HGF treated animals have significantly enhanced levels of remyelination compared to untreated controls.

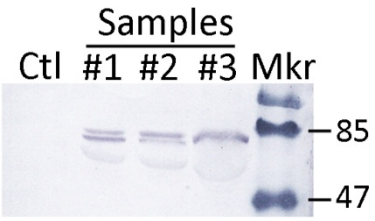

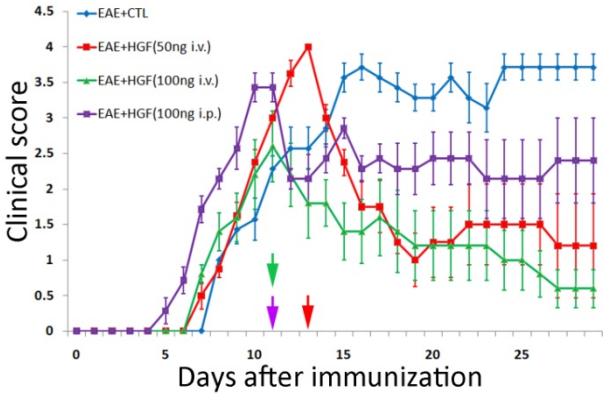

Based on the longitudinal studies, we conducted the first image-guided myelin repair therapy in a rat model of focal demyelination to monitor myelin changes in the spinal cord and determine the dose response of HGF, a multifunctional growth factor that has been proven to be the effective component in MSC therapy of myelin repair (Figure 18, Bai et al., 2012). In this study, rats were first treated with LPC to induce demyelination in the spinal cord. On days 7 and 9, the rats were sequentially treated with HGF, and imaged by [^{11}C]MeDAS-PET on days 7, 14, and 21. At a dose of 100 ng/rat or 0.4 μg/kg, the HGF-treated rats displayed an increased [^{11}C]MeDAS uptake in the spinal cord compared to the control rats. Quantitative analysis showed the HGF treatment caused the average uptake in the demyelinated regions to be 31% and 14% greater at day 14 and 21 respectively, when compared with day 7 (Figure 19). When the rats were treated with a higher dose of HGF (i.e. 200 ng/rat or 0.8 ug/kg), the maximal remyelinating effect was observed to be 33% and 35% on days 14 and 21, respectively. Note there is only a significant difference in the amount of remyelination on day 21, on day 14 the difference in remyelination provided by the additional dose of HGF is not significant. The imaging results were confirmed by double-blinded immunohistochemical observations of postmortem tissue sections harvested at each time point (Bai et al., 2012).

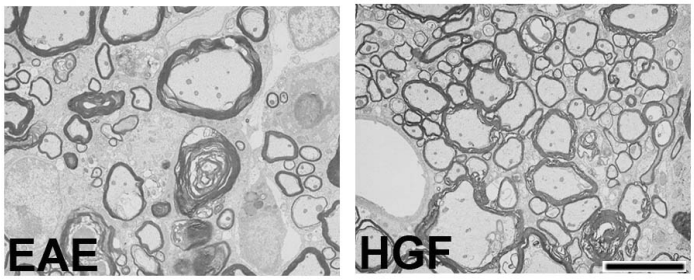

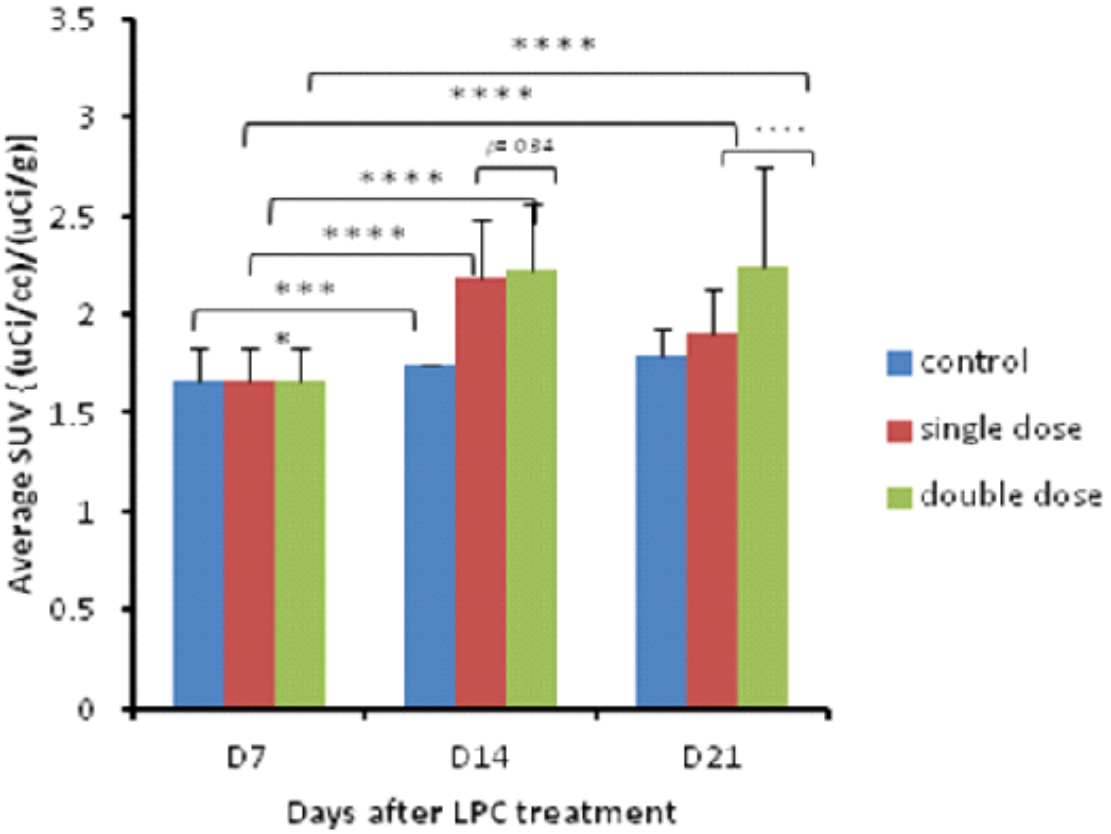

Figure 19. Longitudinal quantitative PET analysis of myelin changes in the spinal cord (T11-12) of a LPC-treated rat model on Day 7, 14, and 21 following HGF-treatment. Increased specific uptake of [^{11}C]MeDAS in spinal cords of HGF treated versus control. Following HGF treatment at a dose of 100 ng/rat or 0.4 ug/kg, the average uptake of [^{11}C]MeDAS increased by 31% and 14% compared to the control on day 14 and 21, respectively. When the HGF dose were doubled, the average uptake of [^{11}C]MeDAS increased by 33% and 35% compared to the control on day 14 and 21, respectively.

3.2.f. Rodent-based dosimetry estimates of [^{11}C]MeDAS

In order to conduct future characterization of [^{11}C]MeDAS in humans, rodent-based dosimetry of [^{11}C]MeDAS was estimated. The single organ and whole body radiation exposure associated with [^{11}C]MeDAS injection was determined from the biodistribution data obtained in mice. Based on the biodistribution, dosimetry was estimated using OLINDA/EXM(Stabin et al., 2005) software. Based on an extrapolation of the animal data to humans, the radiation doses estimated for various human organs are summarized in Table 1.

Target Organ	mSv/MBq	rem/mCi
Adrenals	4.31E-03	1.59E-02
Brain	1.89E-03	7.01E-03
Breasts	2.25E-03	8.34E-03
Gallbladder Wall	3.28E-03	1.21E-02
LLI Wall	3.03E-03	1.12E-02
Small Intestine	3.10E-03	1.15E-02
Stomach Wall	2.93E-03	1.08E-02
ULI Wall	3.06E-03	1.13E-02
Heart Wall	2.30E-03	8.49E-03
Kidneys	2.72E-03	1.00E-02
Liver	4.64E-03	1.72E-02
Lungs	2.91E-03	1.08E-02
Muscle	2.60E-03	9.61E-03
Ovaries	3.12E-03	1.15E-02
Pancreas	3.15E-03	1.16E-02
Red Marrow	3.62E-03	1.34E-02
Osteogenic Cells	6.76E-03	2.50E-02
Skin	2.14E-03	7.92E-03
Spleen	2.41E-03	8.94E-03
Testes	2.58E-03	9.53E-03
Thymus	2.69E-03	9.94E-03
Thyroid	2.69E-03	9.94E-03
Urinary Bladder Wall	2.99E-03	1.11E-02
Uterus	3.14E-03	1.16E-02
Total Body	2.85E-03	1.05E-02
Effective Dose Equivalent	3.30E-03	1.22E-02
Effective Dose	2.99E-03	1.10E-02

Table 1. Organ and whole body extrapolated human dosimetry estimation.

Acute Toxicity study

Following dosimetry estimation, we also evaluated the acute toxicity in mice. A total of 30 mice were divided into 5 groups, which were injected with escalating doses ranging from 82 mg/kg to 168 mg/kg. Based on the survival percentage, we calculated the LD_{50} of MeDAS as 141 mg/kg, which is well in the safety margin, as it is in the 6 orders of magnitude higher than the amount needed for the *in vivo* PET imaging studies.

3.3.a Discussion

With the resources provided by this Synergistic Idea Award from the Department of Defense we have advanced the development of imaging agents for myelin repair to a strong preclinical platform. While there needs to be additional studies to complete the preclinical work we have identified a number of probes that have slightly different characteristics, but may prove useful in analyzing disease burden in multiple sclerosis and other diseases of the nervous system. Multiple sclerosis is the most common of the adult CNS demyelinating diseases. Early in the disease it is characterized by episodes of functional relapse and remission. The biological basis of the relapses and remission is currently unclear. Histological studies imply that intervals of remission are a reflection of remyelination although there is no direct evidence to support this hypothesis. Indeed, relatively little is known about the timing and regulation of

CNS remyelination and until the last 5 years there was relatively little effort focused on developing therapies targeted at myelin repair. As a result current therapeutic strategies primarily target the immune-pathological basis of demyelination and the outcome from this approach has not been particularly successful, as most therapies continue to be directed toward widespread immuno-suppression, and do little to promote long lasting repair. As such, they are of limited value for supporting long-term functional restoration. For long term functional recovery in patients with MS and related acquired demyelinating diseases, more recent efforts have been made to utilize the information generated from patho-biological studies on the development of myelinating oligodendrocyte to identify targets and characterize new therapeutic approaches towards promoting lasting remyelination in the adult CNS.

For drug discovery and development in myelin repair therapy, one major challenge has been assessing and quantifying changes in myelin content *in vivo*. To date, magnetic resonance imaging (MRI) has been the primary tool for diagnosing and monitoring the demyelinating conditions in MS. Unfortunately, any change in signal intensity on a dual echo T2-weighted sequence reflects a change in tissue water content, which is a non-specific measure of the overall changes in macroscopic tissue injury and ranges from edema and inflammation, to demyelination and axonal loss. As a result, MRI changes do not specifically reflect changes in demyelination and remyelination and it cannot be used to unambiguously identify effective remyelinating therapies. It is thus essential to develop a measure that will effectively correlate clinical outcomes directly with myelin content. For this reason, we propose to detect and quantify myelin changes based on PET. PET imaging is a noninvasive imaging technique capable of direct characterization and quantification of biological processes at the molecular level (Phelps, 2000). It has become one of the most important clinical techniques in the diagnosis, prognosis, and monitoring of disease progression. This powerful imaging technique is used in conjunction with trace amounts of positron-emitting radiotracers that are specific for targets of interest.

For *in vivo* detection and quantification of myelin changes, radiotracers must readily enter the brain and specifically bind to myelin sheaths. To date, lack of myelin-specific imaging radiotracers has hampered the application of PET in monitoring demyelination and remyelination. As a result, PET study in MS is limited to the characterization of neuroinflammation using [^{18}F]FDG for glucose metabolism or [^{11}C]PK11195 for peripheral benzodiazepine receptors (PBR) mediated microglia activation (Cuzner, 1997; Wilms et al., 2003; Chen and Guilarte, 2006; Buck et al., 2012). However, such radiotracers are not specific for the characterization of demyelination and remyelination, so they do not provide any correlation of disease progression in MS. Most recently, a F-18 labeled mitochondrial 18kDa translocator protein (TSPO) radioligand termed [^{18}F]DPA-714, has also been developed to image microglial/macrophage activation present in the experimental autoimmune encephalomyelitis (EAE) rat model (Abourbeh et al., 2012). Similar to PBR, TSPO only identifies neuroinflammation (Winkeler et al.; Banati, 2002; Dolle et al., 2009). Thus, [^{18}F]DPA-714 PET can only be used for imaging inflammation, not myelination.

A new strategy is to develop therapeutic agents that are aimed at stimulating remyelination in damaged neural tissues. To date, the development of such myelin repair therapeutics for MS has been hampered by the lack of imaging approaches that allow for direct detection and quantification of myelin changes in a longitudinal manner. In order to meet this challenge, we developed a series of radiotracers for PET imaging of myelination. To identify the most promising PET imaging markers for downstream clinical studies, we used the following set of quantitative acceptance criteria to guide our evaluation processes: 1) High brain uptake at

early time points following i.v. injection. At 5 min post injection, the brain concentration of probe should reach 5% ID/g; 2) Average retention in white matter should be at least 20% higher than that in the adjacent gray matter in the spinal cord; 3) In animal models of MS, radioactivity concentration in demyelinated regions should be significantly lower than that in non-demyelinated regions, based on the same size of regions of interest; 4) Radioactive metabolites in plasma should be hydrophilic, and not permeable across the BBB to avoid diluting the specific uptake signal; 5) Rapid clearance of radiotracer from other organs (e.g., lung, heart, liver, etc.) to ensure optimal dosimetry; 6) Minimal probe toxicity with an LD50 ≥10 mg/kg, or 1,000 times higher than the amount to be injected in future human subjects to ensure a wide margin of safety.

The candidate molecule that best fits these characteristics is [^{11}C]MeDAS that exhibits a promising profile of *in vivo* binding properties and toxicity. Biodistribution studies showed that it readily entered the brain at early time points with 6.07 ID/g at 5 min. After entering the brain, [^{11}C]MeDAS was proportionally localized in the white matter vs. gray matter. In the brain, the average retention in the white matter is ca. 40% higher than in the gray matter. In demyelinated regions, the uptake of [^{11}C]MeDAS was significantly decreased. In the model of focal demyelination introduced by LPC, for example, [^{11}C]MeDAS uptake was 34% lower in the demyelinated regions compared to intact myelinated regions in the spinal cord. Further studies showed that the radioactive metabolites of [^{11}C]MeDAS are hydrophilic and expected not to be permeable across the BBB to interfere with the specific uptake signal. Based on the bio-distribution studies, the dosimetry of [^{11}C]MeDAS was estimated, and these data sets were all well fit with single exponential functions. Most organs appear to receive around 0.002-0.005 mGy/MBq. The total exposure resulting from a 10 mCi administration of [^{11}C]MeDAS is far below the FDA-defined limits for yearly cumulative and per study exposures to research participants, and is comparable with other radiotracers widely used in the clinic. Acute toxicity studies also showed that [^{11}C]MeDAS was safe for potential human studies, with a LD_{50} of 141 mg/Kg or 6 order of magnitude higher than the actual dose needed for PET imaging studies in humans.

It is unlikely that HGF would ever be approved as a systemically delivered therapy for MS due to the potential for tumorogenesis. In this program, however we have used it in the context of a model therapy with which to test that [^{11}C]MeDAS has the potential to identify potential CNS remyelinating therapies. To that end we have performed proof-of concept studies that demonstrate the ability of the probe to detect therapy-induced remyelination in a longitudinal manner. These data, combined with the characterization of [^{11}C]MeDAS binding in the EAE model suggest that the levels of demyelination and remyelination in spinal cord of animals with EAE are considerably more dynamic in both time and location than had been previously appreciated. By analogy, it may well be that current imaging modalities are missing much of the dynamic nature of adult demyelinating diseases and as such fail to provide clarity on the true nature of the disease and its temporal/spatial fluctuations.

CONCLUSION

The studies described above represent a unique imaging-guided approach to monitor disease and repair processes in demyelinating conditions in the CNS, with the absence of invasive surgeries or biopsies. The major advance in being able to utilize our newly developed myelin-imaging technique to quantify local levels of myelination, will for the first time, allow the development of therapeutics that are directly focused at recovery of lost neural tissue. Because myelin repair is critical for sustained functional recovery, the ability to directly track myelin

levels in defined regions of the human CNS will allow us to assess the efficacy of new therapeutics in promoting myelin repair. Thus, the threshold for developing new MS therapeutics will be significantly reduced, and this application holds the promise of allowing new therapeutic development to proceed in a highly accelerated manner. As a consequence, the impact on MS patients will be profound as this novel approach could potentially revolutionize therapeutic development for demyelinating diseases, and hasten their widespread clinical application.

REFERENCES

Abourbeh G, Theze B, Maroy R, Dubois A, Brulon V, Fontyn Y, Dolle F, Tavitian B, Boisgard R (2012) Imaging microglial/macrophage activation in spinal cords of experimental autoimmune encephalomyelitis rats by positron emission tomography using the mitochondrial 18 kDa translocator protein radioligand [(1)(8)F]DPA-714. J Neurosci 32:5728-5736.

Bai L, Lennon DP, Caplan AI, DeChant A, Hecker J, Kranso J, Zaremba A, Miller RH (2012) Hepatocyte growth factor mediates mesenchymal stem cell-induced recovery in multiple sclerosis models. Nat Neurosci 15:862-870.

Banati RB (2002) Visualising microglial activation in vivo. Glia 40:206-217.

Buck D, Forschler A, Lapa C, Schuster T, Vollmar P, Korn T, Nessler S, Stadelmann C, Drzezga A, Buck AK, Wester HJ, Zimmer C, Krause BJ, Hemmer B (2012) 18F-FDG PET detects inflammatory infiltrates in spinal cord experimental autoimmune encephalomyelitis lesions. J Nucl Med 53:1269-1276.

Chen MK, Guilarte TR (2006) Imaging the peripheral benzodiazepine receptor response in central nervous system demyelination and remyelination. Toxicol Sci 91:532-539.

Cuzner ML (1997) Microglia in health and disease. Biochem Soc Trans 25:671-673.

Dolle F, Luus C, Reynolds A, Kassiou M (2009) Radiolabelled molecules for imaging the translocator protein (18 kDa) using positron emission tomography. Curr Med Chem 16:2899-2923.

Kerstetter AE, Padovani-Claudio DA, Bai L, Miller RH (2009) Inhibition of CXCR2 signaling promotes recovery in models of multiple sclerosis. Exp Neurol 220:44-56.

Miller RH, (2002) Regulation of oligodendrocyte development in the vertebrate CNS. Progress in Neurobiology, 67:451-467

Mi S, Hu B, Hahm K, Luo Y, Kam Hui ES, Yuan Q, Wong WM, Wang L, Su H, Chu TH, Guo J, Zhang W, So KF, Pepinsky B, Shao Z, Graff C, Garber E, Jung V, Wu EX, Wu W (2007) LINGO-1 antagonist promotes spinal cord remyelination and axonal integrity in MOG-induced experimental autoimmune encephalomyelitis. Nat Med 13:1228-1233.

Phelps ME (2000) Positron emission tomography provides molecular imaging of biological processes. Proc Natl Acad Sci U S A 97:9226-9233.

Stabin MG, Sparks RB, Crowe E (2005) OLINDA/EXM: the second-generation personal computer software for internal dose assessment in nuclear medicine. J Nucl Med 46:1023-1027.

Stankoff B, Wang Y, Bottlaender M, Aigrot MS, Dolle F, Wu C, Feinstein D, Huang GF, Semah F, Mathis CA, Klunk W, Gould RM, Lubetzki C, Zalc B (2006) Imaging of CNS myelin by positron-emission tomography. Proc Natl Acad Sci U S A 103:9304-9309.

Wang C, Wu C, Zhu J, Miller RH, Wang Y (2010a) Design, synthesis, and evaluation of coumarin-based molecular probes for imaging of myelination. J Med Chem 54:2331-2340.

Wang C, Popescu DC, Wu C, Zhu J, Macklin W, Wang Y (2010b) In situ fluorescence imaging of myelination. J Histochem Cytochem 58:611-621.

Wang C, Wu C, Popescu DC, Zhu J, Macklin WB, Miller RH, Wang Y (2011) Longitudinal near-infrared imaging of myelination. J Neurosci 31:2382-2390.

Wang Y, Wu C, Caprariello AV, Somoza E, Zhu W, Wang C, Miller RH (2009) In vivo quantification of myelin changes in the vertebrate nervous system. J Neurosci 29:14663-14669.

Wenk GL, McGann-Gramling K, Hauss-Wegrzyniak B, Ronchetti D, Maucci R, Rosi S, Gasparini L, Ongini E (2004) Attenuation of chronic neuroinflammation by a nitric oxide-releasing derivative of the antioxidant ferulic acid. J Neurochem 89:484-493.

Wilms H, Claasen J, Rohl C, Sievers J, Deuschl G, Lucius R (2003) Involvement of benzodiazepine receptors in neuroinflammatory and neurodegenerative diseases: evidence from activated microglial cells in vitro. Neurobiol Dis 14:417-424.
Winkeler A, Boisgard R, Martin A, Tavitian B Radioisotopic imaging of neuroinflammation. J Nucl Med 51:1-4.
Wu C, Wei J, Tian D, Feng Y, Miller RH, Wang Y (2008) Molecular probes for imaging myelinated white matter in CNS. J Med Chem 51:6682-6688.
Wu C, Zhu J, Baeslack J, Zaremba A, Hecker J, Kraso J, Matthews PM, Miller RH, Wang Y. Longitudinal PET imaging for monitoring myelin repair in the spinal cord. Ann Neurol. 2013 Jul 1.